

Summary Report of JEM-EUSO Workshop at KICP in Chicago

James H. Adams Jr.,¹ Luis A. Anchordoqui,² Mario Bertaina,³ Mark J. Christl,⁴ Valerie Connaughton,¹ Steven E. Csorna,⁵ Toshikazu Ebisuzaki,⁶ Gustavo Medina-Tanco,⁷ Angela V. Olinto,⁸ Thomas Paul,^{2,9} Piergiorgio Picozza,¹⁰ Andrea Santangelo,¹¹ Kenji Shinozaki,⁶ Thomas J. Weiler,⁵ and Lawrence Wiencke¹²

¹*CSPAR, University of Alabama in Huntsville, Huntsville, AL 35805, USA*

²*Department of Physics, University of Wisconsin-Milwaukee, Milwaukee, WI 53201, USA*

³*Dipartimento di Fisica Generale, Università di Torino, Torino, Italy*

⁴*Marshall Space Flight Center, Huntsville, AL 35812, USA*

⁵*Department of Physics and Astronomy, Vanderbilt University, Nashville TN 37235, USA*

⁶*RIKEN Advanced Science Institute, 2-1 Hirosawa, Wako 351-0198, Japan*

⁷*Instituto de Ciencias Nucleares, UNAM, Ciudad Universitaria, México D.F. 04510, México*

⁸*Department of Astronomy and Astrophysics, University of Chicago, Chicago, IL 60637, USA*

⁹*Department of Physics, Northeastern University, Boston, MA 02115, USA*

¹⁰*INFN, Sezione di Roma Tor Vergata, I-00133 Rome, Italy*

¹¹*Institut für Astronomie und Astrophysik, Eberhard-Karls Universität Tübingen, Tübingen, Germany*

¹²*Department of Physics, Colorado School of Mines, Golden, CO 80401, USA*

(Dated: March 2012)

This document contains a summary of the workshop which took place on 22–24 February 2012 at the Kavli Institute of Cosmological Physics at the University of Chicago. The goal of the workshop was to discuss the physics reach of the JEM-EUSO mission and how best to implement a global ground based calibration system for the instrument to realize the physics goal of unveiling the origin of the highest energy cosmic rays.

I. INTRODUCTION

Ultra high energy cosmic rays (UHECRs) are one of the most enigmatic phenomena in the universe. Despite the fact that the existence of particles with energies reaching 10^{20} eV has been known for over 50 years [1], their origin continues to be an intriguing puzzle [2–7].

Soon after the microwave echo of the big bang was discovered, Greisen [8], Zatsepin, and Kuzmin [9] (GZK) noted that the relic photons make the universe opaque to cosmic rays (CRs) of sufficiently high energy. This occurs, for example, for protons with energies beyond the photopion production threshold,

$$E_{p\gamma\text{CMB}}^{\text{th}} = \frac{m_\pi(m_p + m_\pi/2)}{\omega_{\text{CMB}}} \approx 6.8 \times 10^{19} \left(\frac{\omega_{\text{CMB}}}{10^{-3} \text{ eV}} \right)^{-1} \text{ eV}, \quad (1)$$

where m_p (m_π) denotes the proton (pion) mass and $\omega_{\text{CMB}} \sim 10^{-3}$ eV is a typical photon energy of the cosmic microwave background (CMB). After pion production, the proton (or perhaps, instead, a neutron) emerges with at least 50% of the incoming energy. This implies that the nucleon energy changes by an e -folding after a propagation distance $\lesssim (\sigma_{p\gamma} n_\gamma y_\pi)^{-1} \sim 15$ Mpc [10–13]. Here, $n_\gamma \approx 410 \text{ cm}^{-3}$ is the number density of the CMB photons, $\sigma_{p\gamma} > 0.1$ mb is the photopion production cross section, and y_π is the average energy fraction (in the laboratory system) lost by a nucleon per interaction. For heavy nuclei, the giant dipole resonance can be excited at similar total energies and hence, for example, iron nuclei do not survive fragmentation over comparable distances [14–21]. Additionally, the survival

probability for extremely high energy ($\approx 10^{20}$ eV) γ -rays (propagating on magnetic fields $\gg 10^{-11}$ G) to a distance d , $P(> d) \approx \exp[-d/6.6 \text{ Mpc}]$, becomes less than 10^{-4} after traversing a distance of 50 Mpc [22]. This implies that the GZK sphere represents a small fraction of the size of the universe.¹ Consequently, if the CR sources are universal in origin, the energy spectrum should have a greatly reduced intensity beyond $E \sim E_{\text{GZK}} \equiv 6 \times 10^{19}$ eV, a phenomenon known as the GZK suppression.

The CR spectrum spans over roughly 11 decades of energy. Its shape is remarkably featureless, with little deviation from a constant power law ($J \propto E^{-\gamma}$, with $\gamma \approx 3$) across this large energy range. In 2007, the HiRes Collaboration reported a suppression of the CR flux above $E = [5.6 \pm 0.5(\text{stat}) \pm 0.9(\text{syst})] \times 10^{19}$ eV, with 5.3σ significance [23]. The spectral index of the flux steepens from 2.81 ± 0.03 to 5.1 ± 0.7 . The discovery of the suppression has been confirmed by the Pierre Auger Collaboration, measuring $\gamma = 2.69 \pm 0.2(\text{stat}) \pm 0.06(\text{syst})$ and $\gamma = 4.2 \pm 0.4(\text{stat}) \pm 0.06(\text{syst})$ below and above $E = 4.0 \times 10^{19}$ eV, respectively (the systematic uncertainty in the energy determination is estimated as 22%) [24].

In 2010, an updated Auger measurement of the energy spectrum was published [25], corresponding to a surface array exposure of $12,790 \text{ km}^2 \text{ sr yr}$. This measurement, combining both hybrid and surface detector (SD)-only

¹ The sphere within which a source has to lie in order to provide us with UHECRs if the primaries are subject to the GZK phenomenon.

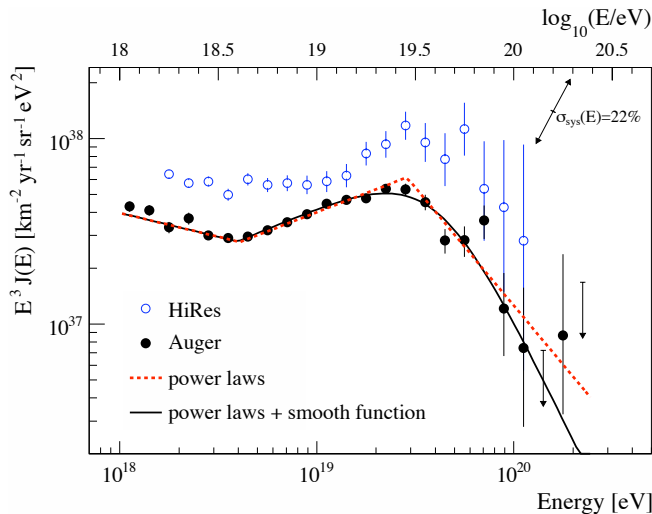


FIG. 1: Combined spectrum from Auger (hybrid and SD events) and the stereo spectrum HiRes. The Auger systematic uncertainty of the flux scaled by E^3 , due to the uncertainty of the energy scale of 22%, is indicated by arrows. The results of the two experiments are consistent within systematic uncertainties. From Ref. [25].

events, is shown in Fig. 1. The so-called “ankle” feature and the flux suppression are clearly visible. A broken power law fit to the spectrum shows that the break corresponding to the ankle is located at $\log_{10}(E/\text{eV}) = 18.61 \pm 0.01$ with $\gamma = 3.26 \pm 0.04$ before the break and $\gamma = 2.59 \pm 0.02$ after it. The break corresponding to the suppression is located at $\log_{10}(E/\text{eV}) = 19.46 \pm 0.03$. Compared to a power law extrapolation, the significance of the suppression is greater than 20σ .

The extreme energy ($E \geq E_{\text{GZK}}$) cosmic ray (EECR) flux is consequently exceptionally low, of the order of 1 *particle/km²/sr/century*. At the high end of the spectrum, $E > 10^{20}$ eV, it reduces to about 1 *particle/km²/sr/millennium*! This challenging extreme energy region is the scope of the Extreme Universe Space Observatory (EUSO) attached to the Japanese Experiment Module (JEM) on board the International Space Station (ISS) [26].

Currently the leading observatories of EECRs are ground based observatories that cover vast areas with particle detectors overlooked by fluorescence telescopes. The largest is the Pierre Auger Observatory in Argentina with a surface detector array of 1600 water Cherenkov tanks covering 3,000 km² which accumulates annually about 6×10^3 km² sr yr of exposure [27]. The more recently constructed Telescope Array (TA) covers 700 km² with 507 scintillator detectors [28], which should accumulate annually about 1.4×10^3 km² sr yr of exposure.

Although extremely large, current observatories are not large enough to study EECRs with the necessary statistics. JEM-EUSO will observe over 4×10^4 km² sr yr at E_{GZK} and reaches 100% exposure around 10^{20} eV where it observes 6×10^4 km² sr yr annually [29, 30],

a factor of 10 above Auger. With a launch date planned for 2017, JEM-EUSO will accumulate 3×10^5 km² sr yr by 2022 in Nadir mode or it can reach the target of 10^6 km² sr yr during the same period in a Tilted mode.

A significant increase in exposure is needed to identify the first sources of UHECRs which should make a clear imprint in the sky at extreme energies (above E_{GZK}). Anisotropies in the distribution of arrival directions of EECRs are a consequence of the GZK suppression. The GZK effect limits the distance from which sources of extreme energy hadrons can contribute to the flux on Earth to below ~ 100 Mpc [31, 32]. The distribution of matter within this distance from Earth is anisotropic, therefore the sky distribution of EECRs should also be anisotropic, modulo the effect of extragalactic magnetic fields. For proton primaries, the anisotropy should be apparent around E_{GZK} , while for higher charged heavier nuclei the anisotropy pattern should become apparent at higher energies, as discussed in Sec. III below.

JEM-EUSO will be the first mission to observe UHECRs from space. This pioneering mission may be the first to clearly identify a source of UHECRs by observing a significantly larger number of EECRs. The source signature will be observed both through the details of the anisotropic distribution of arrival directions as well as the detailed shape of the spectrum above E_{GZK} . Both observations will answer the question of whether the observed spectral suppression is the GZK effect or the maximum energy of UHECR accelerators. Once a clear source is identified, a space based program can be developed to observe the ten million EECR particles that reach the Earth’s atmosphere every year.

II. JEM-EUSO MISSION

JEM-EUSO is an innovative *pathfinder* space mission that will exploit the Earth’s atmosphere as a detector of cosmic ray showers. The remote-sensing space instrument would orbit the Earth every ~ 90 minutes on the ISS at an altitude $h_{\text{ISS}} = 350 - 400$ km. The EUSO instrument is a 2.5 meter telescope with a high-speed ultraviolet (UV) camera ($2.5 \mu\text{s}$ resolution) that will observe the nighttime atmosphere below the ISS with a 60° field of view (FOV) [30, 33]. It will monitor an area larger than 1.3×10^5 km² recording video clips of fast UV flashes by sensing the fluorescence light produced through charged particle interactions (see Fig. 2). This fluorescence is detectable in the 300–400 nm range. JEM-EUSO will have about 3×10^5 pixels each with less than 3 mm that cover about 560 m on the ground.

When the incident cosmic ray interacts with the atomic nuclei of air molecules it produces extensive air showers (EAS) which spread out over large areas (see e.g. [34, 35]). JEM-EUSO will image light from isotropic nitrogen fluorescence excited by the EAS, and forward-beamed Cherenkov radiation reflected from the Earth’s surface or dense cloud tops. The video recorded by JEM-

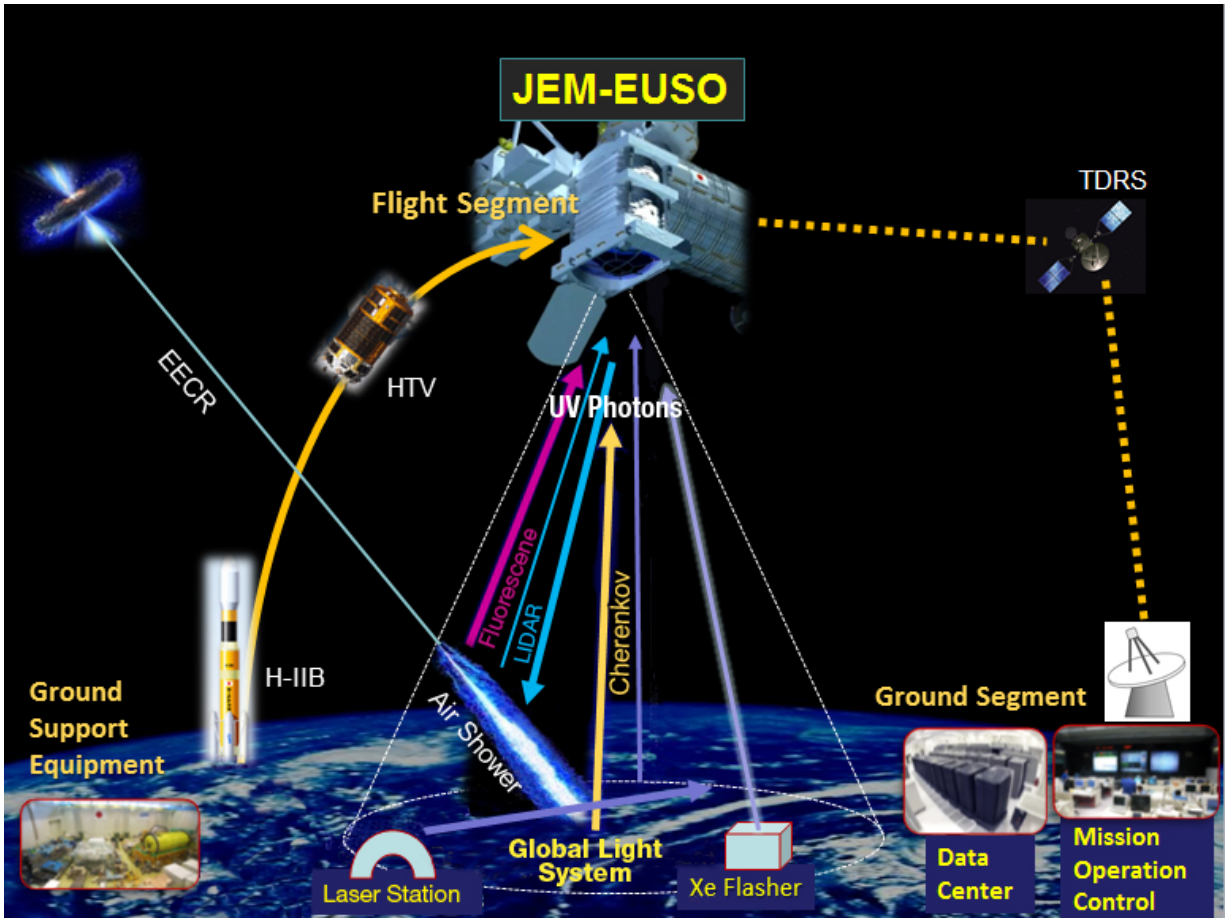


FIG. 2: JEM-EUSO overview and concept of mission operations.

EUSO can capture the moving track of the fluorescent UV photons and reproduces the temporal development of EAS. The instrument will be calibrated using ground-based lasers and Xe flashers. Description of such a calibration procedure is postponed to Sec. V.

Fluorescence observations of the longitudinal development of EAS can give a good estimate of the energy, since the fluorescence light is (in principle) proportional to the electromagnetic (electrons, positrons, and photons) component of the shower which gives a calorimetric estimate of the shower energy. The longitudinal development also has a well defined maximum, usually referred to as X_{\max} , which increases with primary energy as more cascade generations are required to degrade the energy of the secondary particles. The nature of the primary is harder to determine due to large fluctuations of the first interaction point, but the average depth of shower maximum, $\langle X_{\max} \rangle \propto \ln(E/A)$ where A is the mass of the primary cosmic ray nucleus of energy E , can be related to the primary mass through a comparison with hadronic interaction models [36]. A number of alternative methods for mass determinations have also been used based both on the longitudinal development of the fluorescence signal

and the lateral distributions of particles on the ground (see, e.g., [38] for a recent review).

Hadronic interaction models used in describing EAS have to be extrapolated to interactions with center-of-mass energies above 100 TeV, which is well beyond the reach of collider experiments; 14 TeV is the reach of the Large Hadron Collider (LHC). Current models seem to describe recent LHC data well [37] and indicate interesting composition trends at the highest energies [38]. The identification of a clear source of EECRs in the sky will allow for an astrophysical determination of the primary charge of the EECRs which in turn can be used to test the accuracy of hadronic interaction models significantly enlarging the energy reach of experimental tests of particle interactions.

JEM-EUSO will have a reasonable energy resolution, around 30%, while the resolution in X_{\max} will be limited to 120 g/cm^2 which does not allow a separation of different types of nuclei, but can be used to distinguish neutrino and photon events from hadronic events [30, 39, 40]. Many neutrino events have X_{\max} deeper than $2,000 \text{ g/cm}^2$, while most hadronic events have X_{\max} shallower than $2,000 \text{ g/cm}^2$.

In clear air most of the light seen by JEM-EUSO as the shower develops is from nitrogen fluorescence. Nitrogen is excited by the energetic particles in the EAS (almost all of them are electrons). The nitrogen can de-excite in two ways, by collision and by photon emission. At sea level collisional de-excitation dominates. This is because the mean time for de-excitation by photon emission is much longer than the mean time between collisions. As a function of increasing altitude, an increasing fraction of the excited nitrogen de-excites by photon emission because the mean time between collisions decreases with the decreasing atmospheric pressure. Of course, the rate of nitrogen excitation also decreases with atmospheric pressure. The two effects are offsetting, with the result that the fluorescence yield is practically independent of altitude through most of the troposphere.

At higher altitudes, as collisional de-excitation becomes less important, the fluorescence yield (photons per electron per meter traveled in the atmosphere) decreases. This decrease affects the 337 and 357 nm lines first. Because the 391 nm line has a longer fluorescent decay time, the fluorescence yield starts to decrease at a much higher altitude. In most of the troposphere, the fluorescence strength in these three lines is practically equal, but in the upper atmosphere the 391 nm line dominates.

The mechanism for nitrogen fluorescence in EAS has two consequences. First, the fluorescence signal is not a single calorimetric measure of the deposited energy. The EAS must be modeled taking into account the competition between collisional and fluorescent de-excitation (among other effects) to determine the energy of the cosmic ray. JEM-EUSO will not receive a fluorescent signal that is simply proportional to the energy deposited by the EAS.

The second consequence is that the fluorescent signal seen by JEM-EUSO depends on the zenith angle of the EAS. To understand this, consider an EAS near X_{\max} where the number of particles in the shower remains nearly constant. The signal per meter the EAS travels is proportional to the number of particles in the shower. It is easy to see that an inclined shower will reach X_{\max} at a higher altitude where the atmospheric pressure is lower. At such an altitude the shower maximum will be stretched out over a greater distance since its length depends on the grammage traversed by the EAS, not distance. Since the fluorescent signal is proportional to the number of charged particles, the longer distance near shower maximum results in a larger fluorescent signal.

The JEM-EUSO telescope concept is a fast, highly-pixelized, large aperture and wide Field-of-View ($\pm 30^\circ$ FOV) digital camera [33, 41, 42]. In the baseline design the total number of pixels is $\sim 3 \times 10^5$. The angular resolution of each pixel is about 0.07° . For $h_{\text{ISS}} = 400$ km, this resolution corresponds to ~ 0.5 km on the Earth's surface. For each pixel, data is acquired with a time resolution, a.k.a. gate time unit (GTU), of $2.5 \mu\text{s}$. These time-sliced images allow determination of the energy and incoming direction of the primary particle [43].

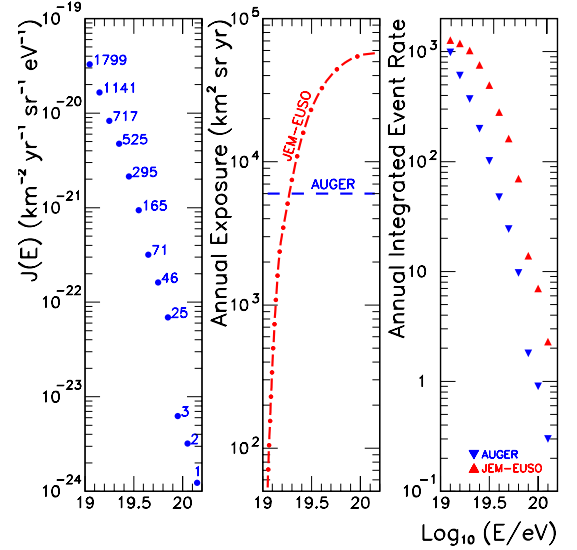


FIG. 3: Left panel: The most recent energy spectrum reported by the Pierre Auger Collaboration [50]. Middle panel: Annual exposure of JEM-EUSO [29] and Auger [27]. Right panel: Estimated event rates derived on the basis of the spectrum in the left panel.

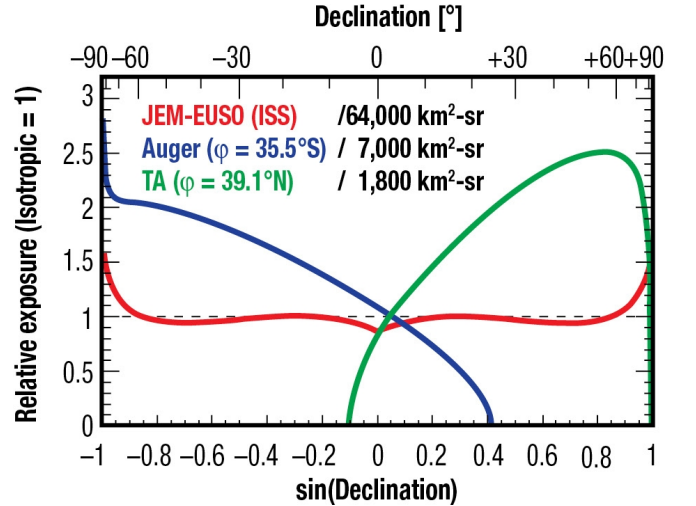


FIG. 4: Normalized relative exposure, $\omega(\sin \delta)$, of Auger, TA, and JEM-EUSO. The latter has a nearly uniform exposure over most of the sky with only small excesses in polar regions.

The observation area of JEM-EUSO depends upon the tilting angle ξ off the nadir and h_{ISS} . For the baseline layout, the observation area for nadir mode is given by

$$A_{\text{obs}}^{(\text{nadir})} \approx 1.4 \times 10^5 \left(\frac{h_{\text{ISS}}}{400 \text{ km}} \right) \text{ km}^2. \quad (2)$$

For tilting angles $\xi \lesssim 40^\circ$,

$$A_{\text{obs}}(\xi) \approx A_{\text{obs}}^{(\text{nadir})} (\cos \xi)^{-b}, \quad (3)$$

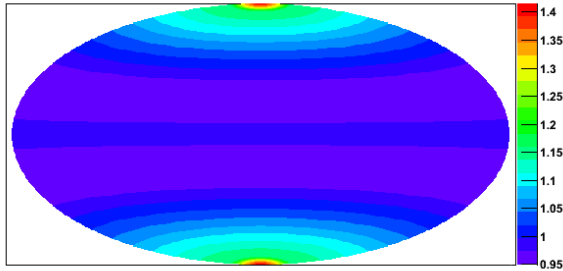


FIG. 5: Sky map in equatorial coordinates showing the relative exposure of JEM-EUSO.

where, for the altitude of interest, $3.2 \leq b \leq 3.4$. For $\xi \sim 40^\circ - 50^\circ$, a part of the FOV views the sky over the local horizon, and A_{obs} saturates above $\xi \sim 60^\circ$.

The UV tracks of EAS must be discriminated in the nightglow background. One key parameter is therefore the fraction of time in which EAS observations are not hampered by the brightness of the sky. The observational duty-cycle η_0 is defined as the fraction of time in which the sky is dark enough to measure EAS. By rescaling measurements of the Tatiana satellite to the ISS orbit, η_0 is estimated to be 19% [30, 44]. In this estimate all major atmospheric effects, such as lightnings, meteors, and anthropic lights (e.g. city lights) have been included.

The impact of clouds is estimated by the global secular statistics of the optical depth and cloud-top altitude [30, 45] convolved with the trigger probability for each case. Applying quality cut for events with shower maximum above the optically thick clouds, this efficiency factor for $E > 3 \times 10^{19}$ eV is estimated to be $\kappa_c \sim 70\%$ (see [30, 46] for details).

The first step to computing the JEM-EUSO geometric aperture involves an estimate of the trigger efficiency. This calculation is performed using a dedicated detector simulation package [30, 47, 48], together with a fast shower simulation allowing for large statistics. Estimates assume the fluorescence yield reported in [49]. The geometric aperture \mathcal{A} is then (conservatively) computed for nadir mode by folding the trigger efficiency with geometrical acceptance for showers of various energies and incident angles, assuming a clear sky condition with average background level [29, 30]. The exposure growth per unit time is given by

$$\frac{d\mathcal{E}}{dt} = \mathcal{A} \eta_0 \kappa_c. \quad (4)$$

In Fig. 3 we show the annual exposure (growth in exposure by one year of operation) together with expected event rate on the basis of the energy spectrum reported by the Pierre Auger Collaboration [50]. This *conservative* event rate will be taken as fiducial throughout this report. However, it is important to keep in mind that the expected event rate would increase by about a factor

of 2 (see Fig. 1) if the spectrum reported by the HiRes Collaboration [23] is taken for normalization of the CR intensity.

The scientific requirements of the mission [51] can be summarized as follows:

- statistical uncertainty on the energy measurement: $\Delta E/E < 30\%$ at $E = 10^{20}$ eV and 60° zenith angle;
- observation area: $A_{\text{obs}}^{(\text{nadir})} \geq 1.3 \times 10^5 \text{ km}^2$ for an orbit height $h_{\text{ISS}} \approx 400 \text{ km}$;
- arrival direction accuracy: better than 2.5° for 60° zenith angle and $E = 10^{20}$ eV;
- accuracy on X_{max} : $\Delta X_{\text{max}} \sim 120 \text{ g cm}^{-2}$ at primary energy $E = 10^{20}$ eV.

Two independent end-to-end simulation packages, “Saitama” developed in Japan and the EUSO Simulation and Analysis Framework (ESAF) [47] developed in Europe, have been used to evaluate the scientific performances of the instrument. In all cases the simulations show that JEM-EUSO will be able to meet these science requirements [52].

Since the ISS orbits the Earth in the latitude range $\pm 51^\circ$, moving at a speed of $\sim 7 \text{ km/s}$, JEM-EUSO will monitor both hemispheres with a rather uniform exposure (see Figs. 4 and 5). This will reduce systematic uncertainties in anisotropy studies. We discuss this next.

III. ANISOTROPY IN ARRIVAL DIRECTIONS

The detection of anisotropies in the distribution of arrival directions will yield the strongest clues to the origin of UHECRs. If cosmic rays are observed to cluster within a small angular region or show directional alignment with powerful compact objects, one might be able to associate them with isolated sources in the sky. Alternatively, if the distribution of arrival directions exhibits a large-scale anisotropy, this would indicate certain classes of sources that are associated with observed large-scale structure (such as the Galactic plane, the Galactic halo, nearby galaxy groups, or the local Supercluster of galaxies).

The lack of clustering on small scales of the currently known 118 events around the extreme energy range (98 from Auger with $E > 5.5 \times 10^{19}$ eV [53] while the Telescope Array reports 20 events with $E > 5.7 \times 10^{19}$ eV [54]) may indicate that either sources are transient, have large number densities, and/or magnetic fields still deflect these particles significantly at these energies [55]. On larger scales, there are hints of anisotropies in the observations of the Pierre Auger Observatory. With the 98 events accumulated until June 2011, Auger reports a 3σ departure from isotropy using a prescription that compares arrival directions with the distribution of nearby active galactic nuclei [53]. The Telescope Array results are consistent with this level of anisotropy. In particular,

the most prominent feature in the UHECR sky is an excess of events in the vicinity of the nearby active galaxy Centaurus A (Cen A).

Anisotropy studies strongly depend on the primary particle species. The smaller magnetic rigidity of heavy nuclei can relax a critical problem faced by current observations, the lack of a suitable clear source in the sky. The lower rigidity (smaller Larmor radius) can lead to significant deflections in typical extragalactic magnetic fields, $\mathcal{O}(\text{nG})$, and would postpone the expected anisotropies in the arrival directions to larger energies.²

Ground-based air shower detectors which experience stable operation over a period of a year or more will have an uniform exposure in right ascension, α . In such a case, the right ascension distribution of the UHECR flux arriving at a detector can be characterized by the amplitudes and phases of its Fourier expansion,

$$I(\alpha) = I_0[1 + r \cos(\alpha - \phi) + r' \cos(2(\alpha - \phi')) + \dots]. \quad (5)$$

For N measurements α_i , the first harmonic amplitude r and its phase ϕ can be determined by applying the classical Rayleigh formalism [59],

$$r = \sqrt{x^2 + y^2}, \quad \phi = \arctan \frac{y}{x}, \quad (6)$$

where

$$x = \frac{2}{N} \sum_{i=1}^N w_i \cos \alpha_i, \quad y = \frac{2}{N} \sum_{i=1}^N w_i \sin \alpha_i, \quad (7)$$

$\mathcal{N} = \sum_{i=1}^N w_i$ is the normalization factor, and the weights, $w_i = \omega^{-1}(\delta_i)$, are the reciprocal of the relative exposure, ω , given in Fig. 4 as a function of the declination, δ_i . As deviations from an uniform right ascension exposure are small, the probability $P(> r)$ that an amplitude equal or larger than r arises from an isotropic distribution can be approximated by the cumulative distribution function of the Rayleigh distribution $P(> r) = \exp(-k_0)$, where $k_0 = \mathcal{N} r^2/4$.

The first harmonic amplitude of the right ascension distribution can be directly related to the amplitude α_d

of a dipolar distribution of the form

$$J(\alpha, \delta) = (1 + \alpha_d \hat{d} \cdot \hat{u}) J_0, \quad (8)$$

where \hat{u} denotes the unit vector in the opposite direction of the shower arrival direction and \hat{d} denotes the unit vector in the direction of the dipole. We can rewrite x , y , and \mathcal{N} as

$$\begin{aligned} x &= \frac{2}{N} \int_{\delta_{\min}}^{\delta_{\max}} d\delta \int_0^{2\pi} d\alpha \cos \delta J(\alpha, \delta) \omega(\delta) \cos \alpha, \\ y &= \frac{2}{N} \int_{\delta_{\min}}^{\delta_{\max}} d\delta \int_0^{2\pi} d\alpha \cos \delta J(\alpha, \delta) \omega(\delta) \sin \alpha, \\ \mathcal{N} &= \int_{\delta_{\min}}^{\delta_{\max}} d\delta \int_0^{2\pi} d\alpha \cos \delta J(\alpha, \delta) \omega(\delta). \end{aligned} \quad (9)$$

In (9) we have neglected the small dependence on right ascension in the exposure. Next, we write the angular dependence in $J(\alpha, \delta)$ as

$$\hat{d} \cdot \hat{u}_i = \cos \delta_i \cos \delta_0 \cos(\alpha_i - \alpha_0) + \sin \delta_i \sin \delta_0, \quad (10)$$

where α_0 and δ_0 are the right ascension and declination of the apparent origin of the dipole, and α_i and δ_i are the right ascension and declination of the i th event. Performing the α integration in (9) it follows that

$$r = \left| \frac{A \alpha_d^\perp}{1 + B \alpha_d^\parallel} \right| \quad (11)$$

where $\alpha_d^\parallel = \alpha_d \sin \delta_0$ is the component of the dipole along the Earth rotation axis, and $\alpha_d^\perp = \alpha_d \cos \delta_0$ is the component in the equatorial plane [60]. The coefficients A and B can be estimated from the data as the mean values of the cosine and the sine of the event declinations,

$$A = \frac{\int d\delta \omega(\delta) \cos^2 \delta}{\int d\delta \omega(\delta) \cos \delta}, \quad B = \frac{\int d\delta \omega(\delta) \cos \delta \sin \delta}{\int d\delta \omega(\delta) \cos \delta};$$

e.g., for the Auger data sample $A = \langle \cos \delta \rangle \simeq 0.78$ and $B = \langle \sin \delta \rangle \simeq -0.45$ [61]. For a dipole amplitude α_d , the measured amplitude of the first harmonic in right ascension r thus depends on the region of the sky observed, which is essentially a function of the latitude of the observatory φ , and the range of zenith angles considered. In the case of a small $B \alpha_d^\parallel$ factor, the dipole component in the equatorial plane is obtained as $\alpha_d^\perp \simeq r/A$. The phase ϕ corresponds to the right ascension of the dipole direction α_0 .³

² Although not generally appreciated, it is important to note that as a statistical average over the sky, an all pervading extragalactic magnetic field is constrained to be $B \lesssim 3 \times 10^{-7} (\Omega_b h^2 / 0.02)^{-1} (h/0.72) (\lambda/\text{Mpc})^{1/2} \text{ G}$, where λ is the coherent length, $\Omega_b h^2 \simeq 0.02$ is the baryon density, and $h \simeq 0.72$ is the present day normalized Hubble expansion rate [56, 57]. This upper limit, derived from measurements of the Faraday rotation in the linearly polarized radio emission from distant quasars [58], depends significantly on assumptions about the electron density profile as a function of redshift [56, 57]. Because Ω_b has contributions from neutrons and only electrons in ionized gas are relevant to Faraday rotation, the previous estimate should be taken as a conservative bound. If extragalactic magnetic fields saturate this upper limit, even EECR protons may suffer large deflections *en route* to Earth [57].

³ A point worth noting at this juncture: A pure dipole distribution is not possible because the cosmic ray intensity cannot be negative in half of the sky. A “pure dipole deviation from isotropy” means a superposition of monopole and dipole, with the intensity everywhere ≥ 0 . An approximate dipole deviation from isotropy could be caused by a single strong source if magnetic diffusion or dispersion distribute the arrival directions over much of the sky. However, a single source would produce higher-order moments as well.

Recently, an intriguing concentration of events has been reported by the Pierre Auger Collaboration [62] in the region around the direction of Cen A, a powerful radiogalaxy at a distance of 3.4 Mpc with equatorial coordinates $(\alpha_0, \delta_0) = (201.4^\circ, -43.0^\circ)$.⁴ Out of the 69 Auger events with $E > 5.5 \times 10^{19}$ eV (collected over 6 yr but equivalent to 2.9 yr of the nominal exposure/yr of the full Auger), the maximum departure from isotropy occurs for a ring of 18° around the object, in which 13 events are observed compared to an expectation of 3.2 from isotropy. The anisotropy amplitude obtained from the 69 arrival directions, assuming a dipole function for a source model with a maximum value at Cen A is found to be $\alpha_d \sim 0.25$ [64].⁵ It is important to keep in mind that this is an *a posteriori* study, so *one cannot use it to determine a confidence level for anisotropy as the number of trials is unknown*.

The right ascension harmonic analyses are completely blind to intensity variations which depend only on declination. Combining anisotropy searches in right ascension over a range of declinations could dilute the results, since significant but out of phase Rayleigh vectors from different declination bands can cancel each other out. A cosmic ray detector with full-sky coverage like JEM-EUSO can exploit standard anisotropy analysis methods that do not work if part of the celestial sphere is never seen. In particular, the distribution of arrival directions can be fully characterized by a set of spherical harmonics coefficients [67, 68]. These coefficients for a function on a sphere are the analogue of Fourier coefficients for a function on a plane. Variations on an angular scale of θ radians contribute amplitude in the $\ell = 1/\theta$ modes just as variations of a plane function on a distance scale of λ contribute amplitude to the Fourier coefficients with $k = 2\pi/\lambda$.

For anisotropy searches at JEM-EUSO, we might look for power in modes from $\ell = 1$ (dipole) out to $\ell \sim 20$, higher order modes being irrelevant because the detector will smear out any true variations on scales that are smaller than its angular resolution. The dipole can be recovered from the celestial intensity function by

$$\alpha_d \hat{d} = \frac{3}{N} \int J(\hat{u}) \hat{u} d\Omega. \quad (12)$$

The components of the dipole vector are found to be

$$\alpha_d d_a = \frac{3}{N} \sum_{i=1}^N \frac{1}{\omega_i} u_a^{(i)}, \quad (13)$$

where $u_a^{(i)}$ denotes a component of the i th vector. (These dipole components are linear combinations of the three spherical harmonic coefficients with $\ell = 1$.)

The sensitivity of JEM-EUSO to a dipole of amplitude α_d can then be estimated via simulation of an ensemble of artificial data sets (with random dipole directions \hat{d}). For each data set, we use the above formula to determine the dipole vector, and record the difference of the estimated α_d from the input dipole amplitude and also the angle between the estimated direction and the input dipole direction. These error distributions describe the measurement accuracy. The RMS deviation from the true α_d is a single number to characterize the amplitude measurement accuracy, and the average space angle error summarizes the accuracy of determining the dipole direction. For a fixed number of arrival directions N , the RMS error in the amplitude has little dependence on the amplitude. For the purpose of detecting an anisotropy (as opposed to measuring it), the relevant quantity is the amplitude divided by the RMS error, which is the number of sigmas deviation from isotropy [67]

$$\frac{\alpha_d}{\Delta\alpha_d} \approx 0.65 \alpha_d \sqrt{N}. \quad (14)$$

It is straightforward to see that *after 3 yr of operation the JEM-EUSO mission will collect about 410 events above 5.5×10^{19} eV providing an “a priori” test for a dipole anisotropy with amplitude $\alpha_d = 0.25$ (for a source model with a maximum value at Cen A) at the 3.3σ level. If the observed excess of events recorded by the Pierre Auger Observatory is not a statistical fluctuation, in 5 yr of JEM-EUSO operations the significance would be increased up to 4.2σ . To reach the standard 5σ discovery level about 1,000 events would be required.*

IV. NEUTRINO SENSITIVITY

In addition to studying the highest energy cosmic rays, JEM-EUSO is also capable of observing extreme energy cosmic neutrinos (EEC ν 's). At present, the IceCube telescope at the South Pole holds the record for the most energetic neutrino interactions observed [69]; these events have energies up to $\sim 10^{14}$ eV and are consistent with the predicted spectrum of atmospheric neutrinos. JEM-EUSO, by contrast, can detect neutrinos with energies $E_\nu \gtrsim 10^{20}$ eV.

The flux of high energy ($E_\nu > 10^{12}$ eV) neutrinos at Earth is expected to be very faint and their interactions with matter are very rare (the interaction length of multi-TeV neutrinos is of the order of the Earth's diameter). Therefore, neutrino telescopes have to face the enormous challenge of observing and identifying very rare neutrino interactions in huge detection volumes [70]. Secondary charged particles produced in weak interactions of neutrinos with nuclei can be identified by Cherenkov light emission in optically transparent media. This method has been successfully applied in Lake Baikal [71]

⁴ The potential of Cen A to accelerate both protons and heavy nuclei in the outer regions of the giant radio lobes has been recently discussed in [63].

⁵ If the observed excess is produced by heavy nuclei accelerated at Cen A, then a larger anisotropy would be expected at $E \sim 10^{18}$ eV [65]. The lack of “low energy” anisotropy in the Auger data sample constrains the spectral index of the potential nucleus emission spectrum [66].

, the Mediterranean (ANTARES [72]) and the Antarctic glacier (AMANDA [73, 74], IceCube [75, 76]). Coherent radio Cherenkov emission has been studied from the regolith of the Moon (GLUE [77]), in the Greenland ice sheet (FORTE [78]) and in the Antarctic ice (RICE [79], ANITA [80, 81]).

At sufficiently high energies cosmic neutrinos can trigger atmospheric air showers similar to those due to high energy cosmic rays (baryons or photons). Although greatly reduced by $\sigma_{\nu N} \approx 6 \times (E_\nu/\text{GeV})^{0.358}$ pb at $E_\nu \gtrsim 10^{20}$ eV [82], the neutrino interaction length

$$L = 1.7 \times 10^7 \left(\frac{\text{pb}}{\sigma_{\nu N}} \right) \text{ kmwe} \quad (15)$$

is far larger than the Earth's atmospheric depth, which is only 0.36 kmwe even when traversed horizontally. Neutrinos therefore produced EAS uniformly at all atmospheric depths. As a result, the most promising neutrino signal are quasi-horizontal showers initiated deep in the atmosphere [83]. For showers with large enough zenith angles, the likelihood of interaction is maximized and the background from baryonic cosmic rays is eliminated, since these showers begin high in the atmosphere. Ground-based cosmic ray observatories (HiRes [84], Auger [85–87], and TA) can also identify neutrino events as electromagnetic showers from Earth-skimming tau-neutrinos [88–90]. As explained in Sec. II, neutrino induced showers recorded by the JEM-EUSO mission can also be distinguished from those of protons and nuclei by requiring that they be *deeply penetrating* [39].

Despite the large experimental effort, neutrino telescopes have yet to identify the first extragalactic neutrino source and so far only place upper bounds on their fluxes. In Fig. 6 we show a summary of diffuse neutrino limits from the various experiments mentioned above. In combining these limits we assume that the total neutrino flux arrives at Earth with an equal composition of flavors. This is expected from neutrino production via pion decay in weak magnetic fields and subsequent flavor oscillations over cosmological distances.

In addition to the direct neutrino limits shown in Fig. 6, there are various indirect limits arising from the so-called “CR \rightleftharpoons ν connection.” We discuss these next.

It is helpful to envision the CR engines as machines where protons are accelerated and (possibly) permanently confined by the magnetic fields of the acceleration region. The production of neutrons and pions and subsequent decay produces neutrinos, γ -rays, and CRs. If the neutrino-emitting source also produces high energy CRs, then pion production must be the principal agent for the high energy cutoff on the proton spectrum. Conversely, since the protons must undergo sufficient acceleration, inelastic pion production needs to be small below the cutoff energy; consequently, the plasma must be optically thin. Since the interaction time for protons is greatly increased over that of neutrons due to magnetic confinement, the neutrons escape before interacting, and on decay give rise

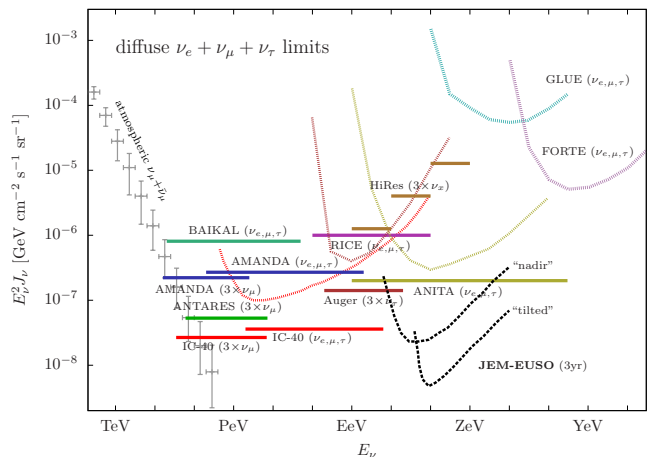


FIG. 6: Summary of diffuse neutrino limits [71–81, 84–87] and the flux of atmospheric neutrinos [69]. For comparison, the EEC ν flux sensitivity of JEM-EUSO (for nadir and tilted modes) to detect 1 event/energy-decade/3 yr is also shown [26].

to the observed CR flux. The foregoing can be summarized as three conditions on the characteristic nucleon interaction time scale τ_{int} ; the neutron decay lifetime τ_n ; the characteristic cycle time of confinement τ_{cycle} ; and the total proton confinement time τ_{conf} : (i) $\tau_{\text{int}} \gg \tau_{\text{cycle}}$; (ii) $\tau_n > \tau_{\text{cycle}}$; (iii) $\tau_{\text{int}} \ll \tau_{\text{conf}}$. The first condition ensures that the protons attain sufficient energy. Conditions (i) and (ii) allow the neutrons to escape the source before decaying. Condition (iii) permits sufficient interaction to produce neutrons and neutrinos. These three conditions together define an optically thin source [91]. A desirable property to reproduce the almost structureless energy spectrum is that a single type of source will produce cosmic rays with a smooth spectrum across a wide range of energy.

The cosmic ray flux above the ankle is often summarized as “one 3×10^{10} GeV particle per kilometer square per year per steradian.” This can be translated into an energy flux [92]

$$\begin{aligned} E \{E J(E)\} &= \frac{3 \times 10^{10} \text{ GeV}}{(10^{10} \text{ cm}^2)(3 \times 10^7 \text{ s}) \text{ sr}} \\ &= 10^{-7} \text{ GeV cm}^{-2} \text{ s}^{-1} \text{ sr}^{-1}. \end{aligned} \quad (16)$$

From this we can derive the energy density ϵ_{CR} in UHE-CRs using flux = velocity \times density, or

$$4\pi \int dE \{E J(E)\} = c \epsilon_{\text{CR}}. \quad (17)$$

This leads to

$$\epsilon_{\text{CR}} = \frac{4\pi}{c} \int_{E_{\text{min}}}^{E_{\text{max}}} \frac{10^{-7}}{E} dE \frac{\text{GeV}}{\text{cm}^2 \text{ s}} \simeq 10^{-19} \frac{\text{TeV}}{\text{cm}^3}, \quad (18)$$

taking the extreme energies of the accelerator(s) to be $E_{\text{min}} \simeq 10^{19}$ eV and $E_{\text{max}} = 10^{21}$ eV. The power

required for a population of sources to generate this energy density over the Hubble time ($\mathcal{T}_H \approx 10^{10}$ yr) is: $\dot{\epsilon}_{\text{CR}}^{[10^{10}, 10^{12}]} \sim 5 \times 10^{44} \text{ TeV Mpc}^{-3} \text{ yr}^{-1} \simeq 3 \times 10^{37} \text{ erg Mpc}^{-3} \text{ s}^{-1}$. This works out to roughly (i) $L \approx 3 \times 10^{39} \text{ erg s}^{-1}$ per galaxy, (ii) $L \approx 3 \times 10^{42} \text{ erg s}^{-1}$ per cluster of galaxies, (iii) $L \approx 2 \times 10^{44} \text{ erg s}^{-1}$ per active galaxy, or (iv) $\int L dt \approx 10^{52} \text{ erg}$ per cosmological gamma-ray burst [92]. The coincidence between these numbers and the observed output in electromagnetic energy of these sources explains why they have emerged as the leading candidates for the CR accelerators.

The energy production rate of protons derived professionally, assuming a cosmological distribution of sources (with injection spectrum typical of shock acceleration $dN_0/dE \propto E^{-2}$) is [93]

$$\dot{\epsilon}_{\text{CR}}^{[10^{10}, 10^{12}]} \sim 5 \times 10^{44} \text{ erg Mpc}^{-3} \text{ yr}^{-1}. \quad (19)$$

This is within a factor of a few of our back-of-the-envelope estimate (1 TeV = 1.6 erg). The energy-dependent generation rate of CRs is therefore given by

$$E^2 \frac{d\dot{n}}{dE} = \frac{\dot{\epsilon}_{\text{CR}}^{[10^{10}, 10^{12}]}}{\ln(10^{12}/10^{10})} \approx 10^{44} \text{ erg Mpc}^{-3} \text{ yr}^{-1}. \quad (20)$$

The energy density of neutrinos produced through $p\gamma$ interactions of these protons can be directly tied to the injection rate of CRs

$$E_\nu^2 \frac{dn_\nu}{dE_\nu} \approx \frac{3}{8} \epsilon_\pi \mathcal{T}_H E^2 \frac{d\dot{n}}{dE}, \quad (21)$$

where ϵ_π is the fraction of the energy which is injected in protons lost into photopion interactions. The factor of 3/8 comes from the fact that, close to threshold, roughly half the pions produced are neutral, thus not generating neutrinos, and one quarter of the energy of charged pion decays goes to electrons rather than neutrinos. Namely, resonant $p\gamma$ interactions produce twice as many neutral pions as charged pions. Direct pion production via virtual meson exchange contributes only about 20% to the total cross section, but is almost exclusively into π^+ . Hence, $p\gamma$ interactions produce roughly equal numbers of π^+ and π^0 . The average neutrino energy from the direct pion decay is $\langle E_{\nu_\mu} \rangle^\pi = (1-r) E_\pi/2 \simeq 0.22 E_\pi$ and that of the muon is $\langle E_\mu \rangle^\pi = (1+r) E_\pi/2 \simeq 0.78 E_\pi$, where r is the ratio of muon to the pion mass squared. In muon decay, since the ν_μ has about 1/3 of its parent energy, the average muon neutrino energy is $\langle E_{\nu_\mu} \rangle^\mu = (1+r) E_\pi/6 \simeq 0.26 E_\pi$.

The ‘‘Waxman-Bahcall (WB) bound’’ is defined by the condition $\epsilon_\pi = 1$

$$E_\nu^2 J_{\text{all } \nu}^{\text{WB}} \approx (3/8) \xi_z \epsilon_\pi \mathcal{T}_H \frac{c}{4\pi} E^2 \frac{d\dot{n}}{dE} \approx 2.3 \times 10^{-8} \epsilon_\pi \xi_z \text{ GeV cm}^{-2} \text{ s}^{-1} \text{ sr}^{-1}, \quad (22)$$

where the parameter ξ_z accounts for the effects of source evolution with redshift, and is expected to be ~ 3 [94].

For interactions with the ambient gas (*i.e.* pp rather than $p\gamma$ collisions), the average fraction of the total pion energy carried by charged pions is about 2/3, compared to 1/2 in the photopion channel. In this case, the upper bound given in Eq. (22) is enhanced by 33%.

The actual value of the neutrino flux depends on what fraction of the proton energy is converted to charged pions (which then decay to neutrinos), *i.e.* ϵ_π is the ratio of charged pion energy to the *emerging* nucleon energy at the source. For resonant photoproduction, the inelasticity is kinematically determined by requiring equal boosts for the decay products of the Δ^+ , giving $\epsilon_\pi = E_{\pi^+}/E_n \approx 0.28$, where E_{π^+} and E_n are the emerging charged pion and neutron energies, respectively. For $pp \rightarrow NN + \text{pions}$, where N indicates a final state nucleon, the inelasticity is ≈ 0.6 [95]. This then implies that the energy carried away by charged pions is about equal to the emerging nucleon energy, yielding (with our definition) $\epsilon_\pi \approx 1$.

At production, if all muons decay, the neutrino flux consists of equal fractions of ν_e , ν_μ and $\bar{\nu}_\mu$. Originally, the WB bound was presented for the sum of ν_μ and $\bar{\nu}_\mu$ (neglecting ν_e), motivated by the fact that only muon neutrinos are detectable as track events in neutrino telescopes. Since oscillations in the neutrino sector mix the different species, we chose instead to discuss the sum of all neutrino flavors. When the effects of oscillations are accounted for, *nearly* equal numbers of the three neutrino flavors are expected at Earth [96].

γ -ray telescopes also constrain the diffuse flux of neutrinos. High energy γ -rays produced in distant sources cannot reach Earth unscathed. At multi-TeV energies γ -rays interact with universal radiation fields, producing e^+e^- pairs. The γ -radiation is recycled to somewhat lower energies by inverse Compton scattering of the electrons and positrons off the same radiation background. These two mechanisms develop electromagnetic cascades until the center-of-mass energy of $\gamma\gamma$ -scattering drops below the pair production (PP) threshold at the order of MeV. For optical photons with energies of the order of eV this occurs at TeV energies. Other processes like synchrotron radiation in extragalactic magnetic fields, double or triple pair production can also contribute to the cascades spectrum. The net result is a pile up of γ -rays at GeV-TeV energies.

The *cascade limit* of diffuse neutrino fluxes is a consequence of the bolometric energy budget of this process [97]. The inferred energy density ω_γ of the extragalactic diffuse γ -ray background in the GeV-TeV region constitutes an upper limit for the total electromagnetic energy from pion production of CR protons.

If the energy loss of pions prior to decay is negligible the neutrino energy relates to the γ -ray energy as $E_\nu \simeq E_\gamma/2$ (per neutrino). The total ν and γ emissivity (Q in units of $\text{GeV}^{-1} \text{s}^{-1}$) from pion decays can then be related by particle number conservation as

$$Q_{\text{all } \nu}(E_\nu) = \frac{3}{2} \frac{\Delta E_\gamma}{\Delta E_\nu} K Q_\gamma(E_\gamma), \quad (23)$$

where the factor K depends on the relative multiplicities of charged and neutral pions, $K = N_{\pi^\pm}/N_{\pi^0}$. There is also one electron from the decay of the muon which contributes as $Q_{\text{all}\nu} \simeq 3Q_e(E_\nu)$. From Eq. (23) with $K = 1$ we have

$$\frac{4\pi}{c} \int dE_\nu E_\nu J_{\text{all}\nu}(E_\nu) \simeq \omega_\nu < \frac{3}{5}\omega_\gamma. \quad (24)$$

The most recent result from Fermi-LAT [98] translates into an energy density of $\omega_{\text{tot}} \simeq 5.8 \times 10^{-7} \text{ eV/cm}^3$ [99, 100]. Assuming an E_ν^{-2} neutrino spectrum between energies E_- and E_+ a numerical simulation gives a cascade limit of [101]

$$E_\nu^2 J_{\text{all}\nu}^{\text{cas}}(E_\nu) \simeq \frac{3 \times 10^{-7}}{\log_{10}(E_+/E_-)} \text{ GeV cm}^{-2} \text{ s}^{-1} \text{ sr}^{-1}. \quad (25)$$

The diffuse neutrino flux has an additional component originating in the energy losses of UHECRs *en route* to Earth [102]. The accumulation of these neutrinos over cosmological time is known as the cosmogenic neutrino flux. The GZK reaction chain generating cosmogenic neutrinos is well known [103]. However, the normalization of the neutrino flux depends critically on the cosmological evolution of the CR sources and on their proton injection spectra [104, 105]. It also depends on the assumed spatial distribution of sources; for example, local sources in the Virgo cluster [106], would dominate the high energy tail of the proton spectrum. Another source of uncertainty is the energy at which there is a transition from Galactic to extragalactic CRs as inferred from a change in the spectral slope [107]. A fourth source of uncertainty is the chemical composition of the parent CRs – if these are heavy nuclei rather than protons, then the neutrino flux is reduced [108–110]. The most up-to-date calculations of the cosmogenic neutrino flux combine a double-fit analysis of the energy and elongation rate measurements to constrain the spectrum and chemical composition of UHECRs at their sources; injection models with a wide range of chemical compositions are found to be consistent with observations [111, 112].

Very recently, duplicating the goodness-of-fit (GOF) test from Ref. [100] optimistic fluxes of cosmogenic neutrinos have been derived through normalization to the Auger spectrum [113]. These optimistic fluxes, shown in Fig. 7, have been presented for a generous range of maximal emission energies $10^{21} \text{ eV} < E_{\text{max}} < 10^{23} \text{ eV}$.⁶ The GOF test of the compatibility of a given model (characterized by the injection spectral index γ and cosmic evolution index n) with the Auger data is shown in Fig. 8. The GOF test with Auger data requires a sharp cutoff at the source on the minimal emission energy of CRs,

$E_{\text{min}} = 10^{19} \text{ eV}$. Such a particular threshold can be explained if, e.g., the sources are optically thin and the ambient optical photon plasma is significantly suppressed, so that $\tau_{\text{int}}(E < E_{\text{min}}) \gg \tau_{\text{int}}(E > E_{\text{min}})$.

Considering the large neutrino fluxes shown in Fig. 7 one might worry about a strong contribution of UHE γ -rays from pion production and a violation of limits on the photon fraction set by Auger [115]. However, this contribution is expected to be dramatically reduced due to PP on the CMB and radio background. Figure 8 shows a comparison of the pair production length on the CMB and the (maximal) radio background of Ref. [114] with the production length of γ -rays via $p\gamma$ interactions on the CMB. (The latter has been estimated as twice the production length of pions, assuming that $E_\gamma \simeq E_p/10$.) The PP interaction length is always much smaller than the production length. Hence, only very local γ -ray sources can contribute with a small fraction to the overall photon fraction (see e.g. Ref. [116]).

Assuming an observational efficiency of 25%, the JEM-EUSO sensitivity to $\text{EEC}\nu$'s has been computed considering both nadir and tilted sky-surveys. As shown in Fig. 6, after 3 yr of running the instrument will be sensitive to neutrino fluxes below the WB and cascade limits. Thus, in principle, if there exists powerful astrophysical sources that are capable of accelerating protons up to $E \sim 5 \times 10^{21} \text{ eV}$, with a power law spectrum $\propto E^{-2}$, JEM-EUSO will be able to observe secondary neutrinos originating in the interactions of these protons both at the source and on their way to Earth.⁷ If we take a more conservative view, in which we try to reproduce the UHECR spectrum measured on Earth and Fermi-LAT observations, the expected $\text{EEC}\nu$ flux yields a prediction just at the threshold of JEM-EUSO observational capacity, see Figs. 6 and 7.

On the other hand, the ability to study neutrino interactions at such extreme energies will open a unique window on possible physics beyond the Standard Model of strong and electroweak interactions. While astrophysical sources (at present level knowledge) can accelerate particles to energies 10^{21} eV at most, topological defects can produce particles, including neutrinos, up to the GUT and Planck scales. Therefore, detection of neutrinos $E_\nu \gtrsim 10^{21} \text{ eV}$ would be a direct signature of physics at energies well beyond the reach of laboratory experiments, such as signatures of topological defects, e.g., the recently proposed [117] string-cusped model.

⁶ By pushing the limit of what it is understood about astrophysical accelerators it is conceivable that E_{max} could extend as high as 10^{23} eV .

⁷ Recall that $E_\nu \sim E/20$.

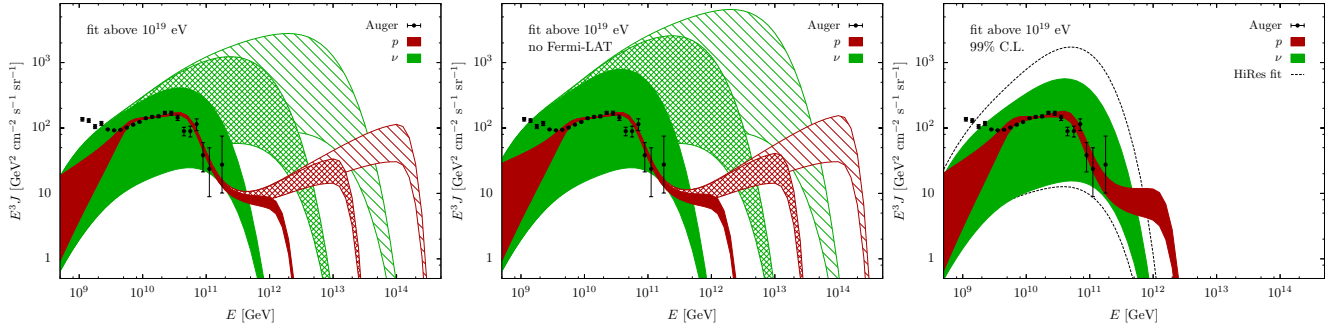


FIG. 7: Optimistic flux of cosmogenic neutrinos consistent with Auger data. The proton and GZK neutrino spectra from the 95% C.L. of the GOF test assuming E_{max} at 10^{21} , 10^{22} and 10^{23} eV are shown in the left and middle panels. The left panel shows neutrino fluxes also consistent with the Fermi-LAT constraint. This constraint is relaxed on the fluxes shown in the middle panel. The right panel shows the proton and GZK neutrino spectra from the 99% C.L. of the GOF test assuming $E_{\text{max}} = 10^{21}$ eV. The dashed lines show the results of [100] for the GZK neutrino flux from a fit to the HiRes data with the same model parameters [113].

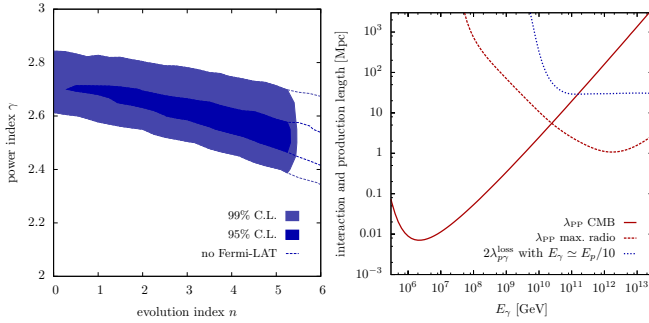


FIG. 8: *Left panel:* Goodness of fit test of the Auger data above 10^{19} eV. The dashed lines show the result without imposing the Fermi-LAT cut on the energy density. *Right panel:* Comparison of the γ -ray production length on the CMB (approximated as twice the total energy loss length in $p\gamma$ interaction with $E_\gamma \simeq E_p/10$) with the PP length of γ -rays in the CMB and radio background [114]. The latter is always smaller than the production length and hence the contribution of γ -rays at high energies is suppressed [113].

V. GLOBAL LIGHT SYSTEM (GLS)

A. Overview

An accurate reconstruction of cosmic ray observables, such as the energy and direction of each event, the shower profile, and the number of events within a given energy, are key for identifying the sources of the highest particles in the universe. To accurately reconstruct these observables, three functions of the pioneering JEM-EUSO instrument are critical:

1. Triggering: How efficiently JEM-EUSO triggers on the optical signatures of EAS and discriminates against background signals.
2. Intrinsic luminosity measurement: How accurately

JEM-EUSO measures the intrinsic luminosity of the EAS. Intrinsic luminosity is determined by applying properly the corrections for geometric, optical, timing, and atmospheric effects.

3. Pointing Accuracy: How accurately JEM-EUSO measures the arrival direction of the EAS over the entire sky.

The JEM-EUSO trigger must become efficient for EAS energies above 3×10^{19} eV. At the same time, the false trigger rate must be low enough for the onboard trigger processing system. To accomplish this, the trigger needs to be tuned carefully for optimum performance under varying atmospheric conditions and background light levels.

The energy of each cosmic ray is determined from the measured intrinsic luminosity of the EAS. Measurements made by JEM-EUSO must be corrected for scattering light in the intervening atmosphere between the ISS and the EAS. The processes for correcting these luminosity measurements and identifying atmospheric regions of the FOV that cannot be used, must be tested in a variety of atmospheric conditions and tuned to minimize the error.

Measurements of each EAS made by JEM-EUSO must be used to reconstruct the EAS trajectory in the atmosphere and used to determine the arrival direction of the cosmic ray in celestial coordinates. This requires not only observing the EAS over a sufficient length in the atmosphere but also correcting for distortion in the optics and pointing errors that result from the flexing of the ISS structure. The pointing accuracy of JEM-EUSO must be checked and the methods for arrival direction reconstruction optimized. Also required are in situ characterizations of the measurement accuracy as a function of time. Factors that vary with time include, for example, atmospheric conditions, background ground light levels, the tilt angle of the detector, and the age of the instrument as it races over the Earth at 28,000 km/h in this pioneering mission.

TABLE I: The GLS will include three types of units.

GLS unit	Sources	#
GLS-X	Xenon Flashlamps (XF)	6
GLS-XL	XF and Laser	6
GLS-AXHL	XF and Horizontal Laser (airborne)	1

An onboard monitoring system of UV light-emitting diodes (LEDs) is operated during daylight segments of the flight when the aperture door is closed. This monitoring function measures any relative variation of individual multi-anode photomultiplier tube (MAPMT) performance and transmission through the lenses during the mission. The atmosphere conditions in the vicinity of an EAS are characterized using JEM-EUSO to measured back-scattered light from an onboard steerable laser. Together these function as a Light Detection And Ranging (LIDAR) system. An IR camera, combined with measurements by JEM-EUSO operating in a slow data acquisition mode, characterize the background photon level, altitude and opacity of any low-lying clouds present. This data, together with a model of the atmosphere and the location and inclination of the EAS, are used to correct for absorption and scattering losses suffered by the fluorescence and Cherenkov photons in each EAS.

The proposed GLS is a worldwide network that combines ground-based Xenon flash lamps and steered UV lasers to provide the most practical and cost-effective alternative to validate the three key parameters (see Table I). The GLS will generate benchmark optical signatures in the atmosphere with similar characteristics to the optical signals of cosmic ray EAS. But unlike air showers, the number, energy, precise time, direction (lasers) can be specified. The local measurement by monitors in the GLS units and the remote measurements made by JEM-EUSO can then be compared. Specifically, JEM-EUSO will reconstruct the pointing directions of the lasers and the intensity of the lasers and flash lamps to monitor the detector's triggers, and accuracy of energy and direction reconstruction. The GLS provides the means to tune the analysis for these atmospheric effects, verify performance of the instrument subsystems (optics, focal surface detector calibration, LIDAR and IR camera, attitude determination) and validate the software and models used in event reconstruction for these space-based observations of EAS.⁸

There will be 12 ground based units strategically placed at sites around the world. Six locations will have flashers and a steerable and remotely operated laser

TABLE II: Candidate locations for deploying GLS.

Location	Latitude	Altitude
Jungfrauoch (Switzerland)	47° N	3.9 km
Mt. Washington (NH, USA)	44° N	1.9 km
Alma-Ata (Kazakhstan)	43° N	3.0 km
Climax (CO, USA)	39° N	3.5 km
Frisco Peak (UT, USA)	38° N	2.9 km
Mt Norikura (Japan)	30° N	4.3 km
Mauna Kea (HI, USA):	20° N	> 3.0 km
Nevado de Toluca (Mexico)	19° N	3.4 km
Chacaltaya (Bolivia)	16° S	5.3 km
La Reunion (Madagascar)	21° S	1.0 km
Cerro Tololo (Chile)	30° S	2.2 km
Sutherland (South Africa)	32° S	1.8 km
Pampa Amarilla (Argentina)	35° S	1.4 km
South Island (New Zealand)	43° S	1.0 km

(GLS-XL) and 6 will have flashers only (GLS-X). Sites will be chosen for their low back-ground light and altitude (above the planetary boundary layer). The placement of GLS units will cover a wide range of terrestrial conditions (land, open ocean) geographical locations, latitudes, and altitudes. It will test the full range of cloud conditions and track trajectories that are encountered in the mission. A nonexclusive list of candidate sites is provided in Table II. We envision placing the 6 GLS-XL units at sites with available grid power, although solar power (as used at Auger) will be considered if the scientific and logistical justification is exceptional and unique. The 12 units will be supplemented by campaign style measurements with an airborne system, that features a Xe flashlamp and a horizontal UV laser. Dubbed the GLS-AXHL, it will be mounted in in P3B Orion aircraft stationed at Wallops Flight Facility/NASA (WFF) in Virginia USA. The GLS-AXHL will be flown over the open ocean at selected altitudes under JEM-EUSO. Details are given in Sec. VD.

In one orbit JEM-EUSO views an area of $1.6 \times 10^7 \text{ km}^2$. Each day JEM-EUSO sweeps over an area of $2.5 \times 10^8 \text{ km}^2$ (which is 83% of Earth's area between $\pm 51.6^\circ$ latitude). On average a GLS site will be over-flown with favorable atmospheric conditions (assuming 10% duty cycle for a ground based station) each day of the mission providing a data base that will be sensitive to seasonal variations at the locations. During an over-flight, the GLS unit will produce calibrated signals repeatedly while in the JEM-EUSO FOV, which last 56 seconds on average.

Our plan addresses the several challenges presented by the GLS. The GLS is developed using Commercial Off-The-Shelf (COTS) components, assembled and tested at the University of Alabama Huntsville (UAH), Colorado School of Mines (Mines) and the Marshall Space Flight Center (MSFC). The fabrication, testing, oper-

⁸ There are no identified UHECR standard candles to provide the convenient references, such as test beams of 10^{20} eV particles. The proposed GLS will provide the best alternative to a test beam.

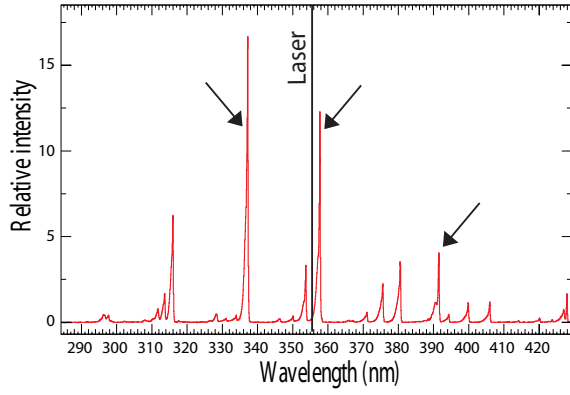


FIG. 9: Measured fluorescence spectrum [122]. The wavelength of the GLS flashers will be filtered to produce light at the lines indicated. The wavelength of the GLS lasers is also shown, (adapted from Ref. [122].)

ations, analysis and maintenance of these units begin only after the mission has been confirmed by the Japan Aerospace Exploration Agency (JAXA) (estimated to occur in 2014). Prior to confirmation by JAXA, the GLS designs will be developed, prototyped and tested. A GLS prototype will support a high-altitude balloon flight in 2014 of a prototype JEM-EUSO telescope, named EUSO-Balloon. The Centre National d'Etudes Spatiales (CNES) is the balloon mission sponsor and this GLS prototype is a key element of this sub-orbital program that will demonstrate the readiness of the technology used for the spaceflight mission. The experience gained during the sub-orbital flight will assure that the GLS design and operations can meet the requirements of the JEM-EUSO spaceflight mission.

B. The Xe-flasher (GLS-X)

Since JEM-EUSO will view the Earth's surface, intrinsic luminosity can be monitored directly with flash lamps. All GLS stations will include four flashlamps, filtered to match the three primary UV fluorescence yield lines [118, 120–122] at 391 nm, 357 nm, and 337 nm (see Fig. 9) and a Schott BG3 wide band-pass filter, identical to that covering the focal plane detector.

The critical functional requirement is a high reliability light flash. Our GLS-X concept incorporates four individual UV-flashers (Hamamatsu L6604) that serve as a set of standard candles. Each flasher is fitted with a mechanical aperture, clear glass outer window, followed by a glass diffuser and one of the optical filters (see Fig. 10). Each flasher includes other ancillary components from Hamamatsu to meet the performance specifications: trigger module, cooling jacket, capacitors for the initial and primary flashes and a power supply. The L6604 has a highly stable output, varying $< 3\%$ from flash-to-flash, long stable lifetime with more than 10^7 flashes and $< 3\%$

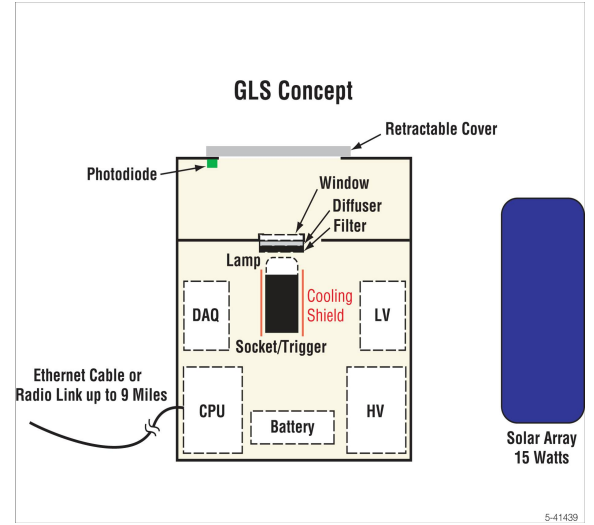
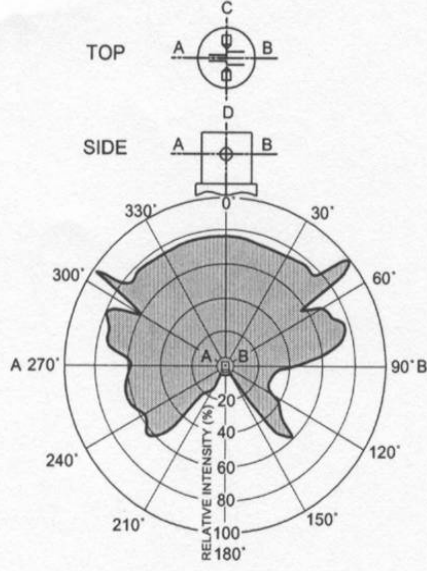
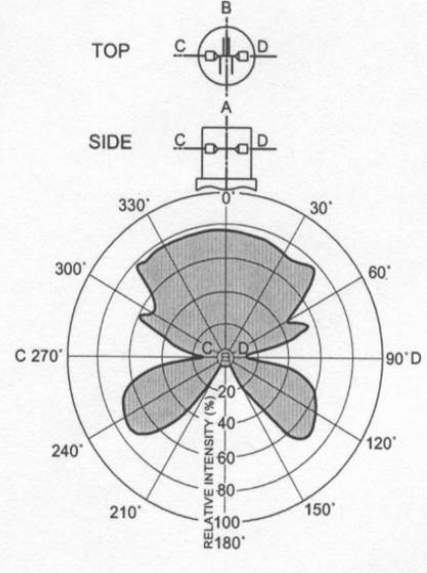


FIG. 10: Diagram of a single GLS-X Concept showing the basic elements.

degradation over the lifetime of the mission [123]. The light pattern from each flash is smoothly distributed over a wide field (see Fig. 11). The intensity of the flash varies slowly over a field $> 60^\circ$ without any spikes or valleys in the intensity. The ripples in the light intensity at the outer fringes of the light field fall outside of the aperture and will not be visible to JEM-EUSO. These key performance parameters have been verified in laboratory tests.

To better match the timing characteristics of a vertical EAS as seen by JEM-EUSO, the light pulse are stretched to > 10 microseconds. This is the minimum acceptable duration for the on-board trigger algorithm and enables JEM-EUSO to detect the GLS-X flashes without requiring a separate dedicated trigger mode. The capacitance and voltage are the principal parameters that control the timing and intensity characteristics of the flashes. We have investigated the performance of the flash lamps for various capacitor values and have succeeded in stretching the pulse while maintaining the stability and repeatability of the light flashes. We verified the performance in the laboratory by analyzing 100 flashes shown in Fig. 12. The data has been converted to photo-electrons detected by the JEM-EUSO instrument based on estimated losses for a clear nighttime atmosphere and the instrument's efficiency factors. The standard deviation for the 100 pulses, measured using the $2.33 \mu\text{s}$ GTU employed in JEM-EUSO, is significantly smaller than the variation expected due to photoelectron statistics for the signal recorded on board; typically 30% smaller. The data in each pixel for successive GTUs are summed together to determine the total signal detected from each GLS-X flash.

The GLS-X flashers are housed in a weather tight enclosure that includes the flasher and its ancillary components, a photo-diode and data acquisition system (DAQ),

Figure 23-1 Light Flux Distribution (1)**Figure 23-2 Light Flux Distribution (2)**

TL8XB0034EA

FIG. 11: Projections of the relative intensity output for the flash lamp. The FOV for JEM-EUSO is restricted to 30° from the vertical where the output is smooth.

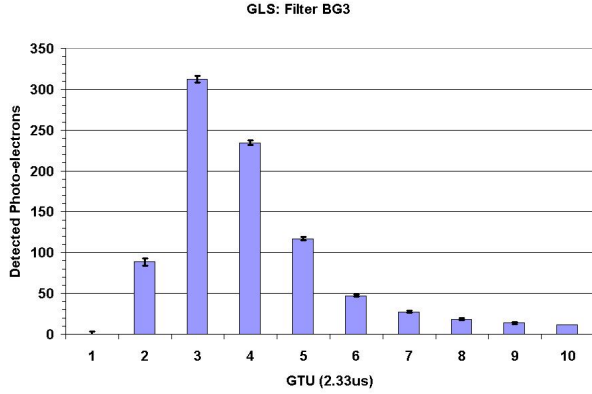


FIG. 12: Measured average intensity of a L6604 flash lamp with a pulsed width stretched to more than 10 μ s. The error bars indicate the standard deviation measured for 100 pulses. The vertical axis is scaled to show the estimated number of photo-electrons detected by JEM-EUSO during each of the 10 GTUs shown.

a mechanical shutter and motor, a single board computer (SBC), solar array and battery (if needed) and a remote communication element (RCE). The RCE provides communication capability with the Central Operations Center (COC) located at the National Space Science and Technology Center (NSSTC) to upload and download parameters for the GLS-X and to retrieve data to determine

its operational status. The RCE will depend on the on-site resources available and will use either a satellite modem or wireless router. The SBC controls the operations of the GLS-X: performs housekeeping functions and reports status to the COC. The GLS-X units are mounted on top of steel poles to minimize potential interferences from the immediate local environment. Discussions with personnel in the US forestry service experienced with remote sensing operations have been used to develop our initial plans for the sites. Members of the international JEM-EUSO Collaboration will provide assistance with identifying candidate sites for the GLS-X and assistance in identifying and communicating with local authorities to assure the operation is free from any interference prior to selecting a site. Table II lists several candidate sites that meet the key requirements for the GLS-X: high elevation and low light pollution.

C. The GLS-XL

Six GLS units will have steered UV laser systems that leverage the successful experiences of the pioneering Fly's Eye [124, 125], HiRes [126–128], and the Pierre Auger Observatory (Auger) [129, 130]. Benchmark data from automated remote lasers [131, 132] in the Auger fluorescence detector (FD) [133] FOV have proven critical both for measuring the performance of the FD [134, 135] and for realizing the science program [136, 137]. There is an approximate effective optical equivalence between

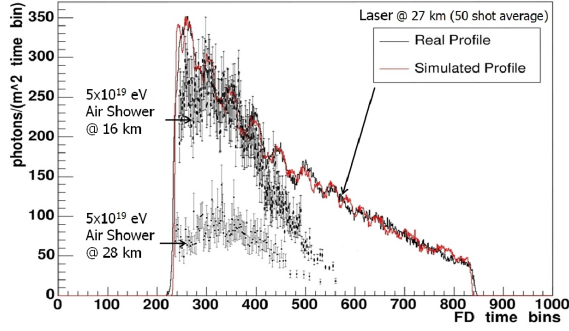


FIG. 13: Longitudinal profiles of vertical laser shots and near-vertical cosmic air showers recorded by the Pierre Auger fluorescence detector from a horizontal distance of 27 km [139]. One time bin is 100 ns. The viewed laser track is 12 km long in this example. The downward going EAS profiles have been flipped so that the left edge of all profiles corresponds to the bottom of the FD field of view.

TABLE III: GLS-XL laser parameters.

Parameter	Specifications
wavelength	355 nm
energy/pulse	1 - 10 mJ
pulse width	10 ns
energy calibration (relative)	3%
energy calibration (absolute)	<10%
pointing (relative)	0.02°
pointing (absolute)	0.2°
timing (absolute)	50 ns

a 5 mJ 355 nm laser track from pulse shot crossing the field of view, and a 10^{20} eV air shower track [138, 139] (see Fig. 13).

A similar equivalence will also apply to JEM-EUSO. In this case both profiles will be elongated in upper part of the troposphere where the air density is less. By adjusting the energy of the laser, the triggering threshold for track-like optical signatures will also be tested. Lasers can also be aimed at UHECR potential sources over the full sky (north and south). A selection of 20 sources could include, for example, the galactic center, Cen A, Virgo, and other objects of astrophysical interest. A sky map of reconstructed laser track directions will be accumulated over the mission. The clusters of points and their spread about the directions of the targeted sources, will provide a simple but comprehensive validation of the absolute EAS pointing accuracy reconstruction by JEM-EUSO. Included in this test is transfer of time stamps from a precise clock on ISS through the JEM-EUSO hardware and the onboard and ground based data analysis chains. During clear periods when 355 nm light propagation in the atmosphere between the GLS site and the ISS can be described to the few percent level using molecular

scattering alone (i.e. aerosol optical depth \ll molecular optical depth), it will be possible to test intrinsic luminosity with both the direct Xe flasher light (point source) and the scattered UV laser light (track source). These periods can be identified by comparing the ratio of flasher measurements at different viewing angles by JEM-EUSO to the ratio predicted by molecular scattering together with measurements of the JEM-EUSO IR camera and onboard laser.

The laser subsystem of the GLS-XL will use many of the components and design features used at the Pierre Auger laser facilities. Proposed specifications are listed in Table III. The laser will be a frequency tripled YAG. Proven models at HiRes and Auger include BigSky (Quantel) CFR and Centurion [119]. The optics will include harmonic separator mirrors to remove residual primary and secondary harmonics. The net polarization of the beam will be randomized so that the atmosphere scatters the same amount of light azimuthally about the beam direction. The steering mechanism will use COTS controller and two orthogonal rotational stages following a design used by Auger and HiRes.

The steering mirrors will be coated for 355 nm and 632 nm reflections so that they can be aligned using a HeNe laser device with an internal pendulum level. These are available at building supply stores. The relative energy of each laser pulse will be measured by directing a small fraction of the beam into a pyroelectric energy probe. The absolute energy of the beam will be calibrated when steering mechanism is parked directing the beam on to a second energy probe mounted inside the system enclosure. To facilitate identification of laser data, the laser will be triggered at precise times referenced to the global positioning system (GPS) timing and the times of each shot recorded locally. Since the laser will be far from the JEM-EUSO detector, the beam will be much narrower than the area viewed by a pixel. Consequently, the beam can be de-collimated significantly to reduce the eye-safe distance.

The system will be housed in a commercially available temperature controlled industrial enclosure/cabinet designed for outdoor use. The steering head will be mounted on top. The laser, optics and controls and other instrumentation will be mounted inside. The entire system will be computer controlled using a single board computer (SBC) with no moving parts. The SBC will be connected to the internet through a firewall computer. Depending on the site a microwave wireless link will be used. (30 km links have been used successfully for many years at the Auger laser systems.) The system will be operated and reprogrammed remotely. The system will include wind, rain, and temperature sensors and a webcam. Past experience has shown that these laser systems are the most stable, and thus provide the most useful benchmark data, when their temperature is controlled (20 ± 5 °C) and the optics are kept free of dust. This compact arrangement, making use of a COTS enclosure is preferred after long experience with other structures.

Consequently, it will be necessary to design and build a GLS-XL prototype and test an entire unit extensively, including the installation and alignment procedures, before finalizing the design and beginning fabrication of the 6 GLS-XL systems planned for the JEM-EUSO ISS mission.

D. Mission Operations

The GLS-to-EUSO interface consists of a trigger pattern that includes the range of intensities and timing characteristics for the GLS. During nominal mission operations, observation planning will be routinely conducted. The resulting plans will be uploaded every few days to the ISS and transferred to EUSO, and executed autonomously. The GLS flashes and tracks will be processed in the same way as EAS triggered events and included in the telemetry stream downloaded to the JAXA operation center and transferred to the JEM-EUSO science center. This data also includes data generated by the onboard Atmospheric Monitoring System (AMS) and the instrument housekeeping data.

The ISS will overfly a GLS-site with favorable weather conditions every night, on average. The ISS ground track speed is 7 km/s and an individual pixel in the focal detector plane has a footprint on the ground of $460 \times 460 \text{ m}^2$ near the nadir for an ISS altitude of 350 km. A GLS site will be in the JEM-EUSO FOV an average of 56 seconds; a pixel crossing time lasts for 60 milliseconds and an average of 1300 pixels will view the GLS site. The GLS-X operates at 10 Hz. The GLS-XLs will alternate laser and flasher pulses, for a total rate of 20 Hz to provide nearly a continuous set of measurements across the JEM-EUSO FOV. For each trigger, the onboard AMS is automatically activated and acquires an IR camera image and a LIDAR shot at the location of the GLS [140]. The signal detected by EUSO under clear sky conditions is estimated to be $> 800 \text{ p.e./ xenon flash}$ [140]. The corresponding estimate for the lasers is $\sim 30 \text{ photons/m}^2$ (at aperture) /pixel/mJ of laser energy (low elevation angle direction) for clear sky conditions. This translates to 500–1000 p.e. per track for 5 mJ laser pulses, depending on the pointing direction. Multiple flashes of the GLS during each over-flight produce transmission estimates with an accuracy of a few percent. The absolute UV attenuation will be determined by analysis and compared with the atmospheric attenuation based on the AMS. There will occasionally be very clear conditions when the measured total optical depth is not significantly greater the molecular optical depth. The latter can be determined accurately [141] from the global data assimilation system (GDAS) [142]. In these cases, the intrinsic luminosity resolution can be measured using track-like signatures by comparing the laser energy as reconstructed by JEM-EUSO and as measured by the GLS-XL energy probe.

The deployment of the GLS will occur prior to the launch in 2017. The 12 ground based sites (6 GLS-

XL, 6 GLS-X) will be selected and the GLS units will be installed and tested. Each site includes a microprocessor or single board computer with internet access, enabling remote management. Operations will be conducted remotely from the COC located at the NSSTC in Huntsville. UAH/MSFC will be responsible for programming the xenon flashers and monitoring their performance. The Colorado School of Mines will be responsible for programming the lasers and monitoring their performance. The ISS times and flash intensity will be pre-loaded for each overpass, when predicted atmospheric conditions are favorable. The pattern of laser shots will be programmed in advance and will include shots fired at potential UHECR sources. After each over-flight, housekeeping data will be relayed to the COC for analysis. Between ISS fly-overs, internal diagnostics will be performed, typically once per day to make sure the systems are functional.

The GLS-AXHL will be installed in a P3B airplane managed by the NASA Airborne Science Program (ASP). The P3B features include an upward viewing portal that is available to install a GLS-X and a side port that will be fitted with a fused silica window to transmit the UV GLS-L pulses. Once the necessary mechanical and electrical interfaces have been developed and tested, the airplane will be deployed approximately monthly for under flights of the ISS at night. The P3B will fly out 500 km from the eastern seaboard to rendezvous with the ISS for a single under-flight. Each flight will target a specific set of conditions. Since the earth rotates by 15 degrees every hour, there will be one ISS overpass per P3B flight. Over the length of the JEM-EUSO mission, these flights will cover a range of altitudes, atmospheric and cloud conditions, and moonlight. The flights will provide sufficient testing for the large number of events acquired by JEM-EUSO over the oceans. After each flight the GLS-AXHL will be dismounted and stored at WFF until the next flight. The details of the P3B flight data will be obtained and included in the analysis of the GLS-AXHL and JEM-EUSO data. The capabilities of the P3B to support the spaceflight mission have been evaluated by the ASP and they have agreed to provide the support needed for these airborne operations.

In addition to validating the accuracy of the EAS reconstruction analysis, the GLS tests the focus of the optical system. The GLS-X serves as a point source and the images of the GLS are small spots with widths that are determined by the optics point-spread function. Throughout the course of the mission, the GLS spot-size will be analyzed to determine if the telescope is maintaining proper focus. The downloaded images of the GLS will be analyzed and compared with optic simulations to guide any focusing adjustments required. Commands can be sent to the telescoping mechanism on JEM-EUSO to adjust the distance between the focal plane and optics to improve the focus.

E. EUSO-Balloon Flight Tests

Balloon flights are planned to demonstrate a prototype of the JEM-EUSO telescope. The EUSO-Balloon mission sponsored by CNES has the following key objectives:

- Full-scale end-to-end test of JEM-EUSO proof of concept and technique.
- Operations of key electronic components including HV control and onboard trigger.
- Acceptance of signals over a large dynamic range.
- Experimental determination of the effective UV background below 40 km.
- Acquisition of JEM-EUSO type data.
- Detection of laser induced events from space.
- Improve trigger algorithms with real data.
- 1st imaging of EAS looking down on the Earth's atmosphere.

A prototype of the GLS-AXHL will be deployed to support the suborbital EUSO-Balloon mission. In addition to providing real experience with supporting an Earth observing EAS detector, the GLS-AXHL will provide critical data for the above listed objectives.

The GLS support for the balloon flights include a ground-based laboratory measurement of the instrument response and an under-flight using the P3B platform with a prototype of the airborne GLS-AXHL planned for the spaceflight mission. Since the balloon will travel more slowly than the aircraft (unlike the ISS), the aircraft can fly multiple passes near the balloon to conduct multiple tests. These exposures will be used to develop the GLS design and to exercise key GLS functions, operations, and analysis for the spaceflight mission. A GLS prototype will be taken to the instrument integration site in France. After completing the integration of the EUSO-Balloon prototype telescope, ground tests will be conducted to assess the overall performance of it. These tests include exposures using LEDs, the dark night sky and bright nighttime sources (moon and stars). The prototype GLS will be one of the sources used in this preliminary performance assessment. In turn, the tests can verify the GLS flash intensity and duration are compatible with the on-board trigger algorithm and dynamic range of the focal plane detector. Preliminary analysis of the acquired data will be completed immediately and a more comprehensive analysis will be completed after the instrument checkout period has been completed. This preliminary exposure will be used to understand the response of the telescope and improve the design of the GLS for the balloon under flight to insure successful operations during the balloon mission.

The P3B platform will be prepared to accommodate the GLS-AXHL for airborne operations. Well in advance

of the balloon flight, the integration and testing (I&T) of the GLS-AXHL will be coordinated with the ASP at NASA/WFF. The upward portal on the P3B will be used for the GLS-X and the sideways viewing port for the GLS-HL. Viewing windows will be installed in the P3B for the GLS-AXHL. A Schott BK7 glass window is baselined because its optical performance meets requirements for the three principal nitrogen fluorescence lines (337, 357 and 391 nm). A quartz window will also be investigated. The I&T includes mechanical fixturing provided by ASP and power resources already existing on the P3B. An engineering flight of the P3B, followed by a 1 hour instrument checkout flight, will be completed at WFF to insure proper installation of the sources. Pre-flight and post-flight ground tests of the GLS-AXHL will be completed to insure they are operational and meet the requirements.

A primary launch site for EUSO-Balloon flights is in Canada. The flight and GLS-AXHL crews will be on stand-by at WFF during the balloon launch window. Once the launch of the EUSO-Balloon instrument is imminent, the P3B will deploy from WFF. The P3B will arrive on site during the nighttime portion of the balloon flight. Once on site and in communication with the ground personnel, the P3B will execute oval flight patterns at preselected altitudes. One leg of the flight path will take the P3B within 1 km of the balloon ground tract where the GLS-X is operated. The other leg of the oval is 10 km distance from the balloon ground track and the laser will shoot across the telescope FOV. The ground personnel will provide feedback in near real-time on the detection of GLS signals to confirm the data acquisition. This balloon mission provides a unique opportunity to exercise and test several elements of the GLS-AXHL system and data analysis for the spaceflight mission. It will be possible to investigate, for example, the impact of the atmosphere in a single location over the range of altitudes spanned by the EAS.

The P3B is our primary option for supporting the spaceflight and balloon flight activities. In the event the P3B will not be available for the balloon launch window, the ASP has alternate aircraft available to support the balloon under-flight at a lower total cost for the planned operations. Additionally, there are several private aviation companies in the vicinity of these remote launch sites that can be evaluated to support the balloon under-flight. There is no issue of availability for the P3B for the spaceflight mission because ISS under-flight opportunities are frequent and can be planned months in advanced.

VI. SUMMARY AND CONCLUSIONS

The JEM-EUSO mission will provide a breakthrough towards the understanding of astrophysical and physical aspects of the universe at extremely high energies. To deeply explore this new face of the cosmos EECR facilities need to observe the full sky and must reach colossal exposures, $\mathcal{O}(10^6 \text{ km}^2 \text{ sr yr})$. Space-based observato-

ries will be a critical element in accomplishing this endeavor. JEM-EUSO is the first step in space: a pioneer and pathfinder in the field.

The high statistics and better experimental handles of the instrument will enable us to locate the CR sources in the sky. The discovery of the first clear source of CRs will be earth-shattering. After more than 50 years, the nature of the strongest cosmic accelerators will be revealed with fundamental consequences for particle astrophysics, including neutrino and gamma ray astronomy. A side benefit of finding nearby CR sources is that the same analysis will provide information on the strength and coherence length of extragalactic magnetic fields.

In addition, the measurement of the shape of the spectrum above E_{GZK} will determine if the steepening observed in the CR intensity is due to the effect of the GZK phenomenon or to the limitations of CR accelerators (E_{max}). To address this ambiguity, JEM-EUSO's high

statistics data set would allow us to observe a spectral recovery above the GZK suppression if $E_{\text{max}} \gg E_{\text{GZK}}$. An optimist might even imagine the discovery of ZeV neutrinos, the telltale signature of universe's topological defects. All in all, we are confident that the pioneering observations of the JEM-EUSO mission will open a new era in CR physics.

Acknowledgements

We thank Markus Ahlers, Paolo Privitera, and Michael Turner for valuable discussions and comments. We are also grateful to Aimee Giles and the Kavli Institute for Cosmological Physics at the University of Chicago for the most enjoyable atmosphere during the Workshop which was funded by an endowment from the Kavli Foundation.

-
- [1] J. Linsley, Phys. Rev. Lett. **10**, 146 (1963).
 - [2] A. M. Hillas, Ann. Rev. Astron. Astrophys. **22**, 425 (1984).
 - [3] M. Nagano and A. A. Watson, Rev. Mod. Phys. **72**, 689 (2000).
 - [4] D. F. Torres and L. A. Anchordoqui, Rept. Prog. Phys. **67**, 1663 (2004) [arXiv:astro-ph/0402371].
 - [5] J. J. Beatty and S. Westerhoff, Ann. Rev. Nucl. Part. Sci. **59**, 319 (2009).
 - [6] K. Kotera and A. V. Olinto, Ann. Rev. Astron. Astrophys. **49**, 119 (2011) [arXiv:1101.4256 [astro-ph.HE]].
 - [7] A. Letessier-Selvón and T. Stanev, Rev. Mod. Phys. **83**, 907 (2011) [arXiv:1103.0031 [astro-ph.HE]].
 - [8] K. Greisen, Phys. Rev. Lett. **16**, 748 (1966).
 - [9] G. T. Zatsepin and V. A. Kuzmin, JETP Lett. **4**, 78 (1966) [Pisma Zh. Eksp. Teor. Fiz. **4**, 114 (1966)].
 - [10] F. W. Stecker, Phys. Rev. Lett. **21**, 1016 (1968).
 - [11] V. S. Berezinsky and S. I. Grigor'eva, Astron. Astrophys. **199**, 1 (1988).
 - [12] F. A. Aharonian and J. W. Cronin, Phys. Rev. D **50**, 1892 (1994).
 - [13] L. A. Anchordoqui, M. T. Dova, L. N. Epele and J. D. Swain, Phys. Rev. D **55**, 7356 (1997) [arXiv:hep-ph/9704387].
 - [14] F. W. Stecker, Phys. Rev. **180**, 1264 (1969).
 - [15] J. L. Puget, F. W. Stecker and J. H. Bredekamp, Astrophys. J. **205**, 638 (1976).
 - [16] L. A. Anchordoqui, M. T. Dova, L. N. Epele and J. D. Swain, Phys. Rev. D **57**, 7103 (1998) [arXiv:astro-ph/9708082].
 - [17] L. N. Epele and E. Roulet, JHEP **9810**, 009 (1998) [arXiv:astro-ph/9808104].
 - [18] F. W. Stecker and M. H. Salamon, Astrophys. J. **512**, 521 (1992) [arXiv:astro-ph/9808110].
 - [19] E. Khan *et al.*, Astropart. Phys. **23**, 191 (2005) [arXiv:astro-ph/0412109].
 - [20] D. Allard, E. Parizot, E. Khan, S. Goriely and A. V. Olinto, Astron. Astrophys. **443**, L29 (2005) [arXiv:astro-ph/0505566].
 - [21] D. Hooper, S. Sarkar and A. M. Taylor, Phys. Rev. D **77**, 103007 (2008) [arXiv:0802.1538 [astro-ph]].
 - [22] J. W. Elbert and P. Sommers, Astrophys. J. **441**, 151 (1995) [arXiv:astro-ph/9410069].
 - [23] R. U. Abbasi *et al.* [HiRes Collaboration], Phys. Rev. Lett. **100**, 101101 (2008) [arXiv:astro-ph/0703099].
 - [24] J. Abraham *et al.* [Pierre Auger Collaboration], Phys. Rev. Lett. **101**, 061101 (2008) [arXiv:0806.4302].
 - [25] J. Abraham *et al.* [Pierre Auger Collaboration], Phys. Lett. B **685**, 239 (2010) [arXiv:1002.1975 [astro-ph.HE]].
 - [26] Y. Takahashi *et al.* [JEM-EUSO Collaboration], New J. Phys. **11**, 065009 (2009) [arXiv:0910.4187 [astro-ph.HE]].
 - [27] J. Abraham *et al.* [Pierre Auger Collaboration], Nucl. Instrum. Meth. A **613**, 29 (2010) [arXiv:1111.6764 [astro-ph.IM]].
 - [28] Y. Tsunesada *et al.* [Telescope Array Collaboration], in Proceeding of the 32nd International Cosmic Ray Conference, Beijing, (ICRC 2011). arXiv:1111.2507 [astro-ph.HE].
 - [29] K. Shinozaki *et al.* [JEM-EUSO Collaboration], in Proceeding of the 32nd International Cosmic Ray Conference, Beijing, (ICRC 2011).
 - [30] J. H. Adams, Jr *et al.* [JEM-EUSO Collaboration], arXiv:1204.5065 [astro-ph.IM].
 - [31] D. Harari, S. Mollerach and E. Roulet, JCAP **0611**, 012 (2006) [arXiv:astro-ph/0609294].
 - [32] D. Allard, E. Parizot and A. V. Olinto, Astropart. Phys. **27**, 61 (2007) [arXiv:astro-ph/0512345].
 - [33] F. Kajino *et al.* [JEM-EUSO Collaboration], in Proceeding of the 32nd International Cosmic Ray Conference, Beijing, (ICRC 2011).
 - [34] L. Anchordoqui, M. T. Dova, A. G. Mariazzi, T. McCauley, T. C. Paul, S. Reucroft and J. Swain, Annals Phys. **314**, 145 (2004) [arXiv:hep-ph/0407020].
 - [35] J. Matthews, Astropart. Phys. **22**, 387 (2005).
 - [36] J. Linsley and A. A. Watson, Phys. Rev. Lett. **46**, 459 (1981).
 - [37] D. d'Enterria, R. Engel, T. Pierog, S. Ostapchenko and K. Werner, arXiv:1106.2453 [hep-ph].

- [38] K. H. Kampert and M. Unger, *Astropart. Phys.*, Topical Issue on Cosmic Rays (2012) [arXiv:1201.0018 [astro-ph.HE]].
- [39] A. D. Supanitsky and G. Medina-Tanco, *Astropart. Phys.* **35**, 8 (2011) [arXiv:1103.4264 [astro-ph.IM]].
- [40] G. Medina-Tanco *et al.* [JEM-EUSO Collaboration], in *Proceeding of the 32nd International Cosmic Ray Conference, Beijing, (ICRC 2011)*.
- [41] F. Kajino *et al.* [JEM-EUSO Collaboration], *AIP Conf. Proc.* **1367**, 197 (2011).
- [42] Y. Kawasaki, M. Casolino, P. Gorodetzky, A. Santangelo, M. Ricci, F. Kajino and T. Ebisuzaki, *AIP Conf. Proc.* **1367**, 201 (2011).
- [43] T. Ebisuzaki *et al.* [JEM-EUSO Collaboration], *AIP Conf. Proc.* **1238**, 369 (2010).
- [44] P. Bobik *et al.* [JEM-EUSO Collaboration], in *Proceeding of the 32nd International Cosmic Ray Conference, Beijing, (ICRC 2011)*.
- [45] F. Garino *et al.* [JEM-EUSO Collaboration], in *Proceeding of the 32nd International Cosmic Ray Conference, Beijing, (ICRC 2011)*.
- [46] G. Sáez Cano *et al.* [JEM-EUSO Collaboration], in *Proceeding of the 32nd International Cosmic Ray Conference, Beijing, (ICRC 2011)*.
- [47] C. Berat *et al.*, *Astropart. Phys.* **33**, 221 (2010) [arXiv:0907.5275 [astro-ph.IM]].
- [48] F. Fenu o *et al.* [JEM-EUSO Collaboration], in *Proceeding of the 32nd International Cosmic Ray Conference, Beijing, (2011)*.
- [49] M. Nagano, K. Kobayakawa, N. Sakaki and K. Ando, *Astropart. Phys.* **22**, 235 (2004) [arXiv:astro-ph/0406474].
- [50] P. Abreu *et al.* [Pierre Auger Collaboration], arXiv:1107.4809 [astro-ph.HE].
- [51] A. Santangelo *et al.* [JEM-EUSO Collaboration], *AIP Conf. Proc.* **1238**, 380 (2010).
- [52] A. Santangelo, F. Fenu, T. Ebisuzaki and K. Shinozaki [JEM-EUSO Collaboration], *Nucl. Phys. Proc. Suppl.* **212-213**, 368 (2011).
- [53] A. V. Olinto, in *Proceedings of 12th International Conference on Topics in Astroparticle and Underground Physics (TAUP 2011)* arXiv:1201.4519 [astro-ph.HE].
- [54] D. Ikeda [for the Telescope Array Collaboration], in *Proceedings of 12th International Conference on Topics in Astroparticle and Underground Physics (TAUP 2011)*.
- [55] P. Abreu *et al.* [Pierre Auger Collaboration], *Astropart. Phys.* **35**, 354 (2012) [arXiv:1111.2472 [astro-ph]].
- [56] P. Blasi, S. Burles and A. V. Olinto, *Astrophys. J.* **514**, L79 (1999) [arXiv:astro-ph/9812487].
- [57] G. R. Farrar and T. Piran, *Phys. Rev. Lett.* **84**, 3527 (2000) [arXiv:astro-ph/9906431].
- [58] P. P. Kronberg, *Rept. Prog. Phys.* **57**, 325 (1994).
- [59] J. Linsley, *Phys. Rev. Lett.* **34**, 1530 (1975).
- [60] J. Aublin, E. Parizot, *Astron. Astrophys.* **441**, 407 (2005).
- [61] P. Abreu *et al.* [Pierre Auger Collaboration], *Astropart. Phys.* **34**, 267 (2011). [arXiv:1103.2721 [astro-ph.HE]].
- [62] P. Abreu *et al.* [Pierre Auger Collaboration], *Astropart. Phys.* **34**, 314 (2010) [arXiv:1009.1855].
- [63] A. Pe'er and A. Loeb, *JCAP* **1203**, 007 (2012) [arXiv:1111.3964 [astro-ph.HE]].
- [64] L. A. Anchordoqui, H. Goldberg and T. J. Weiler, *Phys. Rev. D* **84**, 067301 (2011) [arXiv:1103.0536 [astro-ph.HE]].
- [65] M. Lemoine and E. Waxman, *JCAP* **0911**, 009 (2009) [arXiv:0907.1354].
- [66] P. Abreu *et al.* [Pierre Auger Collaboration], *JCAP* **1106**, 022 (2011) [arXiv:1106.3048 [astro-ph.HE]].
- [67] P. Sommers, *Astropart. Phys.* **14**, 271 (2001) [arXiv:astro-ph/0004016].
- [68] L. A. Anchordoqui, C. Hojvat, T. P. McCauley, T. C. Paul, S. Reucroft, J. D. Swain and A. Widom, *Phys. Rev. D* **68**, 083004 (2003) [arXiv:astro-ph/0305158].
- [69] R. Abbasi *et al.* [IceCube Collaboration], *Phys. Rev. D* **83**, 012001 (2011) [arXiv:1010.3980 [astro-ph.HE]].
- [70] L. A. Anchordoqui and T. Montaruli, *Ann. Rev. Nucl. Part. Sci.* **60**, 129 (2010) [arXiv:0912.1035 [astro-ph.HE]].
- [71] V. Aynutdinov *et al.* [BAIKAL Collaboration], *Astropart. Phys.* **25**, 140 (2006) [arXiv:astro-ph/0508675].
- [72] J. A. Aguilar *et al.* [ANTARES Collaboration], *Phys. Lett. B* **696**, 16 (2011) [arXiv:1011.3772 [astro-ph.HE]].
- [73] A. Achterberg *et al.* [IceCube Collaboration], *Phys. Rev. D* **76**, 042008 (2007) [Erratum-ibid. **D 77**, 089904 (2008)] [arXiv:0705.1315 [astro-ph]].
- [74] M. Ackermann *et al.* [IceCube Collaboration], *Astrophys. J.* **675**, 1014 (2008) [arXiv:0711.3022 [astro-ph]].
- [75] R. Abbasi *et al.* [IceCube Collaboration], *Phys. Rev. D* **83**, 092003 (2011) [Erratum-ibid. **D 84**, 079902 (2011)] [arXiv:1103.4250 [astro-ph.CO]].
- [76] R. Abbasi *et al.* [IceCube Collaboration], *Phys. Rev. D* **84**, 082001 (2011) [arXiv:1104.5187 [astro-ph.HE]].
- [77] P. W. Gorham, C. L. Hebert, K. M. Liewer, C. J. Naudet, D. Saltzberg and D. Williams, *Phys. Rev. Lett.* **93**, 041101 (2004) [arXiv:astro-ph/0310232].
- [78] N. G. Lehtinen, P. W. Gorham, A. R. Jacobson and R. A. Roussel-Dupre, *Phys. Rev. D* **69**, 013008 (2004) [arXiv:astro-ph/0309656].
- [79] I. Kravchenko *et al.*, *Phys. Rev. D* **73**, 082002 (2006) [arXiv:astro-ph/0601148].
- [80] P. W. Gorham *et al.* [ANITA collaboration], *Phys. Rev. Lett.* **103**, 051103 (2009) [arXiv:0812.2715 [astro-ph]].
- [81] P. W. Gorham *et al.* [ANITA Collaboration], *Phys. Rev. D* **82**, 022004 (2010) [Erratum-ibid. **D 85**, 049901 (2012)] [arXiv:1011.5004 [astro-ph.HE]].
- [82] L. A. Anchordoqui, A. M. Cooper-Sarkar, D. Hooper and S. Sarkar, *Phys. Rev. D* **74**, 043008 (2006) [arXiv:hep-ph/0605086].
- [83] K. S. Capelle, J. W. Cronin, G. Parente and E. Zas, *Astropart. Phys.* **8**, 321 (1998) [arXiv:astro-ph/9801313].
- [84] R. U. Abbasi *et al.* [HiRes Collaboration], arXiv:0803.0554 [astro-ph].
- [85] J. Abraham *et al.* [Pierre Auger Collaboration], *Phys. Rev. Lett.* **100**, 211101 (2008) [arXiv:0712.1909 [astro-ph]].
- [86] J. Abraham *et al.* [Pierre Auger Collaboration], *Phys. Rev. D* **79**, 102001 (2009) [arXiv:0903.3385 [astro-ph.HE]].
- [87] P. Abreu *et al.* [Pierre Auger Collaboration], *Phys. Rev. D* **84**, 122005 (2011) [Phys. Rev. D **85**, 029902 (2012)] [arXiv:1202.1493 [astro-ph.HE]].
- [88] J. L. Feng, P. Fisher, F. Wilczek and T. M. Yu, *Phys. Rev. Lett.* **88**, 161102 (2002) [arXiv:hep-ph/0105067].
- [89] X. Bertou, P. Billoir, O. Deligny, C. Lachaud and A. Letessier-Selvon, *Astropart. Phys.* **17**, 183 (2002) [arXiv:astro-ph/0104452].
- [90] D. Fargion, *Astrophys. J.* **570**, 909 (2002) [arXiv:astro-

- ph/0002453].
- [91] M. Ahlers, L. A. Anchordoqui, H. Goldberg, F. Halzen, A. Ringwald and T. J. Weiler, *Phys. Rev. D* **72**, 023001 (2005) [arXiv:astro-ph/0503229].
 - [92] T. K. Gaisser, arXiv:astro-ph/9707283.
 - [93] E. Waxman, *Astrophys. J.* **452**, L1 (1995).
 - [94] E. Waxman and J. N. Bahcall, *Phys. Rev. D* **59**, 023002 (1999) [arXiv:hep-ph/9807282].
 - [95] J. Alvarez-Muniz, R. Engel, T. K. Gaisser, J. A. Ortiz and T. Stanev, *Phys. Rev. D* **66**, 033011 (2002) [arXiv:astro-ph/0205302].
 - [96] J. G. Learned and S. Pakvasa, *Astropart. Phys.* **3**, 267 (1995) [arXiv:hep-ph/9405296].
 - [97] V. S. Berezinsky and A. Y. Smirnov, *Astrophys. Space Sci.* **32**, 461 (1975).
 - [98] A. A. Abdo *et al.* [The Fermi-LAT collaboration], *Phys. Rev. Lett.* **104**, 101101 (2010) [arXiv:1002.3603 [astro-ph.HE]].
 - [99] V. Berezinsky, A. Gazizov, M. Kachelriess and S. Ostapchenko, *Phys. Lett. B* **695**, 13 (2011) [arXiv:1003.1496 [astro-ph.HE]].
 - [100] M. Ahlers, L. A. Anchordoqui, M. C. Gonzalez-Garcia, F. Halzen and S. Sarkar, *Astropart. Phys.* **34**, 106 (2010) [arXiv:1005.2620 [astro-ph.HE]].
 - [101] M. Ahlers, to be published in Proceedings of the Workshop *VLV/T* 2011, Erlangen, Germany.
 - [102] V. S. Berezinsky and G. T. Zatsepin, *Phys. Lett. B* **28**, 423 (1969).
 - [103] F. W. Stecker, *Astrophys. J.* **228**, 919 (1979).
 - [104] S. Yoshida and M. Teshima, *Prog. Theor. Phys.* **89**, 833 (1993).
 - [105] R. Engel, D. Seckel and T. Stanev, *Phys. Rev. D* **64**, 093010 (2001) [arXiv:astro-ph/0101216].
 - [106] C. T. Hill and D. N. Schramm, *Phys. Rev. D* **31**, 564 (1985).
 - [107] Z. Fodor, S. D. Katz, A. Ringwald and H. Tu, *JCAP* **0311**, 015 (2003) [arXiv:hep-ph/0309171].
 - [108] D. Hooper, A. Taylor and S. Sarkar, *Astropart. Phys.* **23**, 11 (2005) [arXiv:astro-ph/0407618].
 - [109] M. Ave, N. Busca, A. V. Olinto, A. A. Watson and T. Yamamoto, *Astropart. Phys.* **23**, 19 (2005) [arXiv:astro-ph/0409316].
 - [110] D. Allard *et al.*, *JCAP* **0609**, 005 (2006) [arXiv:astro-ph/0605327].
 - [111] L. A. Anchordoqui, H. Goldberg, D. Hooper, S. Sarkar and A. M. Taylor, *Phys. Rev. D* **76**, 123008 (2007) [arXiv:0709.0734 [astro-ph]].
 - [112] K. Kotera, D. Allard and A. V. Olinto, *JCAP* **1010**, 013 (2010) [arXiv:1009.1382 [astro-ph.HE]].
 - [113] M. Ahlers and L. A. Anchordoqui, Auger Internal Report GAP-2012-035.
 - [114] R. J. Protheroe and P. L. Biermann, *Astropart. Phys.* **6**, 45 (1996) [Erratum-ibid. **7**, 181 (1996)], [arXiv:astro-ph/9605119].
 - [115] J. Abraham *et al.* [Pierre Auger Collaboration], *Astropart. Phys.* **31**, 399 (2009) [arXiv:0903.1127 [astro-ph.HE]].
 - [116] M. Ahlers and J. Salvado, *Phys. Rev. D* **84**, 085019 (2011) [arXiv:1105.5113 [astro-ph.HE]].
 - [117] V. Berezinsky, E. Sabancilar and A. Vilenkin, *Phys. Rev. D* **84**, 085006 (2011) [arXiv:1108.2509 [astro-ph.CO]].
 - [118] F. Arqueros, J. R. Hoerandel and B. Keilhauer, *Nucl. Instrum. Meth. A* **597**, 1 (2008) [arXiv:0807.3760 [astro-ph]].
 - [119] <http://www.quantel-laser.com/products/item/134.html>
<http://www.quantel-laser.com/products/item/135.html>
 - [120] F. Arqueros, J. R. Hoerandel and B. Keilhauer, *Nucl. Instrum. Meth. A* **597**, 23 (2008) [arXiv:0807.3844 [astro-ph]].
 - [121] M. Ave *et al.* [AIRFLY Collaboration], *Nucl. Instrum. Meth. A* **597**, 50 (2008) [arXiv:0711.4583 [astro-ph]].
 - [122] M. Ave *et al.* [AIRFLY Collaboration], *Astropart. Phys.* **28**, 41 (2007) [arXiv:astro-ph/0703132].
 - [123] Xenon Flash Lamps, Hamamatsu Photonics K.K., <http://www.hamamatsu.co>
 - [124] D. J. Bird *et al.*, *Astrophys. J.* **441**, 144 (1995).
 - [125] R. M. Baltrusaitis *et al.*, *Nucl. Instrum. Meth. A* **240**, 410 (1985).
 - [126] L. R. Wiencke *et al.* [HiRes Collaboration], *Nucl. Instrum. Meth. A* **428**, 593 (1999).
 - [127] L. Wiencke *et al.*, in *Proceedings of SPIE* **3818**, 46 (1999).
 - [128] C. Cannon, L. Pedersen, R. Riehle, J. Thomas and L. Wiencke [for the HiRes Collaboration], in *Proceeding of the 28th International Cosmic Ray Conference, Tsukuba, (ICRC 2003)*, p.477; <http://www-rccn.icrr.u-tokyo.ac.jp/icrc2003/PROCEEDINGS/PDF/120.pdf>
 - [129] L. Wiencke, F. Arqueros, J. Compton, M. Monasor, D. Pilger and J. Rosado, arXiv:1105.4016 [astro-ph.IM].
 - [130] L. Wiencke *et al.* [Pierre Auger Collaboration], in *Proceeding of the 32nd International Cosmic Ray Conference, Beijing, (ICRC 2011)*, [arXiv:1107.4806].
 - [131] B. Fick, M. Malek, J. Matthews, R. Meyhandan, M. Mostafa, M. Roberts, P. Sommers and L. Wiencke *et al.* [Pierre Auger Collaboration], *JINST* **1**, P11003 (2006) [arXiv:astro-ph/0507334].
 - [132] <http://astroserve.mines.edu>
 - [133] J. Abraham *et al.* [Pierre Auger Collaboration], *Nucl. Instrum. Meth. A* **620**, 227 (2010) [arXiv:0907.4282 [astro-ph.IM]].
 - [134] J. Abraham *et al.* [Pierre Auger Collaboration], *Astropart. Phys.* **33**, 108 (2010) [arXiv:1002.0366 [astro-ph.IM]].
 - [135] P. Abreu *et al.* [Pierre Auger Collaboration], *Astropart. Phys.* **34**, 368 (2011) [arXiv:1010.6162 [astro-ph.HE]].
 - [136] J. Abraham *et al.* [Pierre Auger Collaboration], *Phys. Rev. Lett.* **104**, 091101 (2010) [arXiv:1002.0699 [astro-ph.HE]].
 - [137] P. Abreu *et al.* [Pierre Auger Collaboration], arXiv:1107.4804 [astro-ph.HE].
 - [138] L. Wiencke [for the Pierre Auger Collaboration], *Nucl. Instrum. Meth. A* **572**, 508 (2007) [arXiv:astro-ph/0607449].
 - [139] L. Wiencke [for the Pierre Auger Collaboration], *J. Phys. Conf. Ser.* **160**, 012037 (2009) [arXiv:0807.2884 [astro-ph]].
 - [140] J. H. Adams and M. Christl [for the EUSO Collaboration], in *Proceedings of the 28th International Cosmic Ray Conference, Tsukuba, (ICRC 2003)*, p.919; <http://www-rccn.icrr.u-tokyo.ac.jp/icrc2003/PROCEEDINGS/PDF/230.pdf>
 - [141] P. Abreu *et al.* [Pierre Auger Collaboration], *Astropart. Phys.* **35**, 591 (2012) [arXiv:1201.2276 [astro-ph.HE]].
 - [142] NOAA Air Resources Laboratory (ARL), Global Data Assimilation System (GDAS) Archive Information, Tech. Rep. (2004);

<http://ready.arl.noaa.gov/gdas1.php>